Climate Dynamics
https://doi.org/10.1007/s00382-022-06235-y

Reassessing the relative role of anthropogenic aerosols and natural decadal variability in driving the mid-twentieth century global "cooling": a focus on the latitudinal gradient of tropospheric temperature

Chenrui Diao[1] · **Yangyang Xu**[1]

Received: 13 September 2021 / Accepted: 27 February 2022

Abstract
The global mean surface temperature cooled slightly in the mid-twentieth century despite a continuous increase in greenhouse gas concentrations. The cooling was strongest in the Northern Hemisphere mid-latitudes, while the Southern Hemisphere mid-latitudes experienced moderate warming. This apparent contradiction is often attributed to internal multi-decadal variability originating from Pacific and Atlantic ocean-atmosphere interactions. Given the rapid increase of industrial activities in North America and Europe during that period, it is also plausible that anthropogenic aerosol (AA) emissions (as an external forcing) contributed to the stronger Northern Hemisphere cooling. This paper aims to quantify the contributions of AA and decadal variability to the 1948–1978 cooling. We analyzed the latitudinal temperature trend asymmetry in 60° S–60° N throughout the troposphere, using multiple reanalysis datasets and the Coupled Model Intercomparison Project phase 5 (CMIP5) multi-model ensemble that bears significant similarity with the observed patterns. We show that both AA increase and the North Atlantic Variability Index (NAVI) transition into its negative phase are the major contributors to the latitudinal asymmetry of cooling. At the surface level, based on the horizontal pattern correlation method, AA and NAVI have similar contribution fractions (20 vs. 16%), but the contribution fraction of AA is much larger at 500 hPa (55 vs. 8%). Attributions based on vertical pattern correlation and latitudinal gradient show consistent results. Natural forcings (NAT) also contribute to the cooling asymmetry during mid-20C, but with a much smaller impact compared to AA and NAVI. Therefore, we argue that previous studies that mostly focused on surface variables may have underestimated the role of AA in the mid-twentieth-century climate change. The study suggests that the three-dimensional thermal structure and atmospheric circulation change should be closely examined in future climate attribution analysis.

Keywords Anthropogenic aerosol · Decadal climate change · Climate model · Tropospheric temperature · Hemispheric asymmetry

1 Introduction

Despite the continuous increase in greenhouse gases (GHGs) concentrations since the Industrial Revolution (Fig. 1a), global warming is not monotonic in the twentieth century. From about 1998–2013, the global mean surface temperature (GMST) warmed very slowly compared with the rapid warming from about 1978–1997 and is referred to as a global warming "hiatus" (Easterling and Wehner 2009; Kosaka and Xie 2013; Yan et al. 2016). The robustness of the so-called "hiatus" is also questioned in light of observational uncertainties (e.g., Foster and Rahmstorf 2011; Cowtan and Way 2014; Karl et al. 2015; Cheng and Zhu 2014) and statistical significance of trend during a relatively short period (e.g., Medhaug et al. 2017; Risbey et al. 2018; Rahmstorf et al. 2017). In general, the causes of the recent warming slowdown in the early twenty-first century are shown to be related to internal variability and/or aerosol forcings (from industrial or minor volcanic eruptions).

Recent studies demonstrate that oceanic multi-decadal internal variability is the main driver of such decadal

✉ Yangyang Xu
yangyang.xu@tamu.edu

[1] Department of Atmospheric Sciences, Texas A&M University, College Station, TX 77843, USA

Published online: 17 March 2022

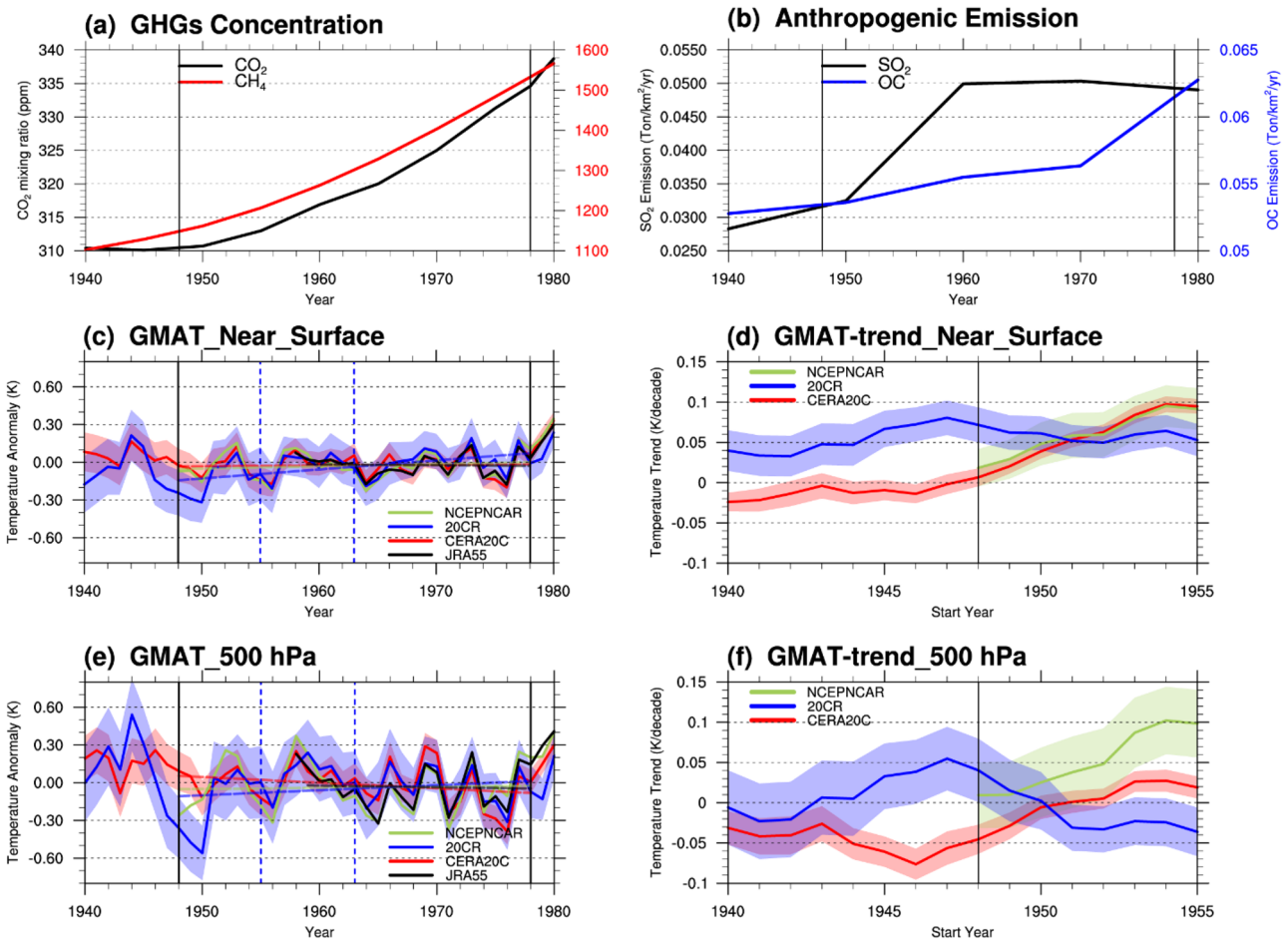

Fig. 1 Evaluation of anthropogenic forcing and global mean air temperature. **a** Global average atmospheric concentrations of CO_2 and CH_4. CO_2 concentration data is provided by NOAA ESRL/GMD; CH_4 concentration is provided by Advanced Global Atmospheric Gases Experiment (AGAGE). The two black vertical lines (1948–1978) in **a**–**c**, and **e** indicate the "mid-20C" period, which is the focus of our analysis. **b** Global Emissions of SO_2 and OC (organic carbon). Emission data is from the historical emission used in CMIP5 twentieth century simulation. More information and data access can be found at https://tntcat.iiasa.ac.at:8743/RcpDb/. **c** The global mean air temperature (GMAT in K, shown as anomaly relative to the 1951–1980 climatology) at the near-surface level. The colored straight lines represent the linear trends of four different reanalysis datasets from 1948 to 1978 (except for JRA55 using 1958–1978). The two blue dashed lines indicate the two volcanic eruption events in 1955 (Bezymianny, Russia) and 1963 (Mount Agung, Indonesia). The blue and red color shadings represent the ensemble uncertainties from CERA20C and 20CR (NCEPNCAR has only one realization). **d** The 31-year GMAT trend (K/decade) for starting years between 1940 and 1955. The black vertical line represents 1948. The blue and green shadings represent the 95% confidence interval of 31-year linear regressions for 20CR and NCEPNCAR; the red shading represents the 95% confidence interval of the 10-member ensemble spread of CERA20C is shown in red shading. **e**, **f** Same as **c**, **d**, but for 500 hPa air temperature

changes in GMST, but debates are ongoing on the relative importance of the Pacific Ocean and the Atlantic Ocean. Some studies demonstrated the dominant role of the Atlantic Multidecadal Variability (AMV) in driving the varying global warming rate, including both the rapid warming periods and the warming slowdown periods (e.g., Knight et al. 2006; Thompson et al. 2010; Mann et al. 2014; Tung and Chen 2018). The variability of Atlantic Meridional Overturning Circulation (AMOC) is proposed to modulate the externally-driven SST variations (e.g., Kostov et al. 2014; Chen and Tung 2018; Zhang et al. 2019; An et al. 2021). In contrast, some other studies argue that Pacific variability, such as the Interdecadal Pacific Oscillation (IPO), is the main driver (Kosaka and Xie 2013; Maher et al. 2014; Dai et al. 2015; Dong and McPhaden 2017).

In addition to internal variability, the external forcing introduced by anthropogenic aerosol (AA) is also suggested to play a major role in causing the warming slowdown (Chang et al. 2010; Booth et al. 2012; Jones et al. 2013; Takahashi and Watanabe 2016; Haustein et al. 2019). Some studies emphasize the combined effects of decadal variability and external forcings during the recent warming

slowdown (e.g., Flato et al. 2013; Fyfe et al. 2016; Medhaug et al. 2017). Furthermore, some recent studies also argue that the external forcing also partly drives the well-known modes of Pacific internal variability (Emile-Geay et al 2008; Dong et al. 2014; Takahashi and Watanabe 2016; Le 2017; Haustein et al. 2019) or Atlantic internal variations (Evan et al. 2009; Otterå et al. 2010), which further increases the complexity of the attribution analysis.

The regularised optimal fingerprint (ROF; Ribes et al. 2013) algorithm is widely used in previous studies to detect and attribute the role of anthropogenic forcings to the global and regional temperature (Bindoff et al. 2013; Sun et al. 2016; Fyfe et al. 2017; Gillet et al. 2021), which utilizes both spatial and temporal fingerprints of responses. Unlike the strong warming effects of GHGs, the anthropogenic aerosol forcings, based on ROF methods, show overall cooling effects but with large uncertainties to the global temperature throughout the twentieth century.

The recent warming slowdown event is not unique in the historical period and should be viewed in the greater context of decadal climate trends during other periods of the twentieth century, which is the focus of this study. GHGs, while strongly contributing to temperature warming, is not the only contributor to the global temperature trend. Natural or anthropogenic forcings such as volcanic eruption and anthropogenic aerosol emission contribute to the cooling tendency (Bindoff et al. 2013). Here we aim to quantify the contributions of external forcing and internal variability to the mid-twentieth century ("mid-20C", defined here as 1948–1978) global "cooling", which was stronger and longer compared with the more recent "hiatus". Specifically, we address to what extent AA emissions, mainly from North America and Europe during this period, contributed to the mid-20C slowdown. A better understanding of the contribution to the slowing down of global warming, will not only improve the understanding of human effects on the past climate (e.g., Liu et al. 2017) but also help to quantify the uncertainty of the future climate projection in the next few decades (Xu and Hu 2018). The novelty of this study lies in the following two aspects.

1. When attributing the causes of the mid-20C slowdown, most previous studies focus on GMST changes but do not fully utilize the spatial pattern of the observed trend, which has a strong hemispheric asymmetry. Unlike globally well-mixed GHGs, AA is largely confined to the emission source regions, thus invoking distinct climate response "fingerprints". A few previous studies connected AA with the hemispheric asymmetry of temperature trend (Cai et al. 2006; Friedman et al. 2013; Haustein et al. 2019) or tropical precipitation shift (Chiang and Friedman 2012; Hwang et al. 2013; Ocko et al. 2014; Allen et al. 2015; Chung and Soden 2017). Similarly, the fingerprint of internal variability originating from different ocean basins could induce different spatial patterns. The novelty in the present work compared to previous ones is that we include both temporal and spatial information into the attribution process. Instead of considering the simple hemispheric differences as in most previous studies, we focus *on the latitudinal asymmetry, expressed in various forms, as the major metric for attribution.*
2. Most previous studies focus on surface properties. However, a few studies (Tett et al. 2002; Thompson et al. 2010) emphasize the importance of anthropogenic sulfate aerosols in offsetting GHG warming in the troposphere. Therefore, here we focus not only on the surface temperature but also on the air temperature throughout the entire troposphere to gain a 3-dimensional perspective of the changes.

The paper is organized as follows. In Sect. 2, we describe the data and statistical methods, and then in Sect. 3, we discuss the observed air temperature trend during the mid-20C. In Sect. 4, we discuss the simulated latitudinal asymmetry of temperature trend during mid-20C and the fingerprints of external forcings and internal variability in detail. In Sect. 5, we attribute the observed hemispheric asymmetry based on multi-model experiments of CMIP5 with three attribution methods (Sects. 5.1–5.4). Then we discuss the model spread and uncertainty based on the aerosol-cloud mechanisms (Sect. 5.4). Section 5 provides a summary.

2 Methods

2.1 Reanalysis datasets

Table 1 shows the three main reanalysis datasets used in this study, including NCEP/NCAR Reanalysis 1 ("NCEP-NCAR") developed by NCEP and NCAR (Kalnay et al. 1996), Coupled European ReAnalysis of the 20th Century ("CERA20C") developed by ECMWF (Laloyaux et al. 2016), and Twentieth Century Reanalysis ("20CR") developed by NOAA (Compo et al. 2011). The observations assimilated are also listed in Table 1. CERA20C provides ten ensemble members, which we use for uncertainty quantification. The ensemble spread for 20CR is also considered for uncertainty analysis.

A fourth reanalysis dataset is the Japanese 55-year Reanalysis ("JRA55"), developed by JMA (Kobayashi et al. 2015), which assimilates multiple sources of observations using a modern assimilation scheme. However, JRA55 has a much shorter temporal coverage (starting only from 1958), so we only consider it to verify temperature trends in the other three main reanalysis datasets (Fig. 1c and e).

Table 1 Reanalysis datasets used in this study, including air temperature at various pressure levels and also air temperature near the surface (2 m)

Full name of Dataset	Short name in the paper	Covered period	Resolution (latitude × longitude)	Assimilated observations	References
NCEP/NCAR Reanalysis 1	NCEPNCAR	1948–present	2.5° × 2.5°	Surface pressure, temperature, wind, and relative humidity vertical temperature, wind and, relative humidity	Kalnay et al. (1996); Kistler et al. (2001); https://psl.noaa.gov/data/gridded/data.ncep.reanalysis.surface.html
20th Century Reanalysis Version 2C	20CR	1851–2014	2.0° × 2.0°	Surface pressure, SST, sea ice	Compo et al. (2011); https://psl.noaa.gov/data/gridded/data.20thC_ReanV2c.html
Coupled European ReAnalysis of the 20th Century	CERA20C	1901–2010	1.0° × 1.0°	Surface pressure, marine wind, ocean temperature	Laloyaux et al. (2016); https://www.ecmwf.int/en/forecasts/datasets/reanalysis-datasets/cera-20c
Japanese 55-year Reanalysis	JRA55	1958–2015	1.25° × 1.25°	Surface pressure, temperature; upper-level temperature, wind, relative humidity	Kobayashi et al. (2015); https://jra.kishou.go.jp/JRA-55/index_en.html

For the four reanalysis datasets, we utilize the monthly mean air temperature data from the surface to the upper troposphere. The data from the four datasets are interpolated to be of the same vertical coordinates (1000–250 hPa at 50 hPa intervals). The data from NCEPNCAR and CERA20C are interpolated to the horizontal grids of 20CR (2.0° × 2.0°) before further analysis. Besides, we also utilize the 2-m air temperature (T2M) to quantify the rates of global warming (Fig. 1).

We omit the polar regions (above 60°) in our latitudinal analyses (except Fig. 1), considering the high surface elevations of the Antarctic ice cap as well as the large Arctic observation uncertainties.

We here define the "mid-20C" period as 1948–1978 for several reasons. First, NCEPNCAR only started in 1948. Using 1948 as the starting year also avoids the problem of limited observation coverage during WWII (Brohan et al. 2006; Thompson et al. 2010). Second, global aerosol forcing went up rapidly (Fig. 1b) during this period, providing a window of opportunity to detect its influence, if any. Third, a period of 31 years is sufficiently long to smooth out short-term variations such as ENSO and volcanic eruptions. Fourth, the rapid global warming period began in the late 1970s (Trenberth and Hurrell 1994), which is beyond the scope of our analysis. Also, as a result of using 1948–1978 as the focus period, other more recent reanalysis datasets assimilating global satellite observations (usually starting in 1979; e.g., MERRA2, ERA5) are not used in this study.

2.2 CMIP5 model experiments

Table 2 lists seven CMIP5 models that include All-forcing (ALL), Greenhouse-gas-only (GHG), Anthropogenic-aerosol-only (AA), natural-forcing-only (NAT) experiments with at least three runs for each experiment. If there are more than three runs from any model, we only use the first three to ensure the multi-model mean (MMM) is not biased toward any single model. An alternative method to calculate MMM is to calculate the average of all ensemble members from each model and then to average across models. However, due to the limited realizations for each model (less than ten), the model-generated internal variability cannot be removed entirely via ensemble averaging. This means that the models with fewer realizations (e.g., three), despite ensemble average, will carry a stronger internally generated trend into the eventual MMM. In contrast, here we pick the same number of realizations from each model and from each experiment (i.e., a total of 21 runs from 7 models for ALL/GHG/AA/NAT experiments) to make sure all these models contribute equally to MMM.

We exclude some other CMIP5 models (e.g., MIROC-ESM, HadGEM2) that lack any of the three required experiments listed above or have fewer than three runs for any

Table 2 Global climate model output from CMIP5 used in this study

Model Name	Main Developer	Resolution (latitude × longitude)	Cloud Albedo effect	Cloud Lifetime effect	Reference
CCSM4	USA/NCAR	0.94° × 1.25°	No	No	Gent et al. 2011
CanESM2	Canada/CCCma	2.79° × 2.81°	Yes	No	Chylek et al. 2011
GISS-E2-R	USA/NASA	2° × 2.5°	Yes	No	Lee et al. 2013
GISS-E2-H	USA/NASA	2° × 2.5°	Yes	No	Lee et al. 2013
CESM1-CAM5	USA/NCAR	0.94° × 1.25°	Yes	Yes	Meehl et al. 2013b
CSIRO-MK3-6-0	Australia/CSIRO	1.87°× 1.875°	Yes	Yes	Collier et al. 2011
GFDL-CM3	USA/GFDL	2° × 2.5°	Yes	Yes	Griffies et al. 2013

Color coding here, consistent with Fig. 9g–i, divides all models into three groups based on the physical parameterization of aerosol indirect effects (see columns 4 and 5)

experiments. Also, we use the first 300 years of Pre-Industrial (PI) experiments to quantify the internal variability (except for GISS-E2-H, which only provides 240 years of PI runs).

Besides the single forcing experiments of GHG, AA, and NAT, a historical (stratospheric + tropospheric) ozone-only experiment (OZ) is also performed by four of the seven included models (GISS-E2-R, GISS-E2-H, CCSM4, and CESM1-CAM5). We again pick the first three realizations from each model (12 runs in total) to analyze the potential role of ozone. CSIRO-MK3-6-0 performed All-but-ozone experiments, where the ozone-induced response can be obtained by contrasting with ALL experiments. However, the ozone-induced response obtained from All-but-ozone experiments is still different from that in ozone-only experiments due to the potential nonlinear relationship between ozone and other external forcings, thus CSIRO-MK3-6-0 is excluded from the ozone analysis. It is worth noting that ozone experiments in CMIP5 include both stratospheric and tropospheric ozone.

As with reanalysis products, we use the monthly mean air temperature at various pressure levels (T) and the 2-m air temperature (T2M) for the model analysis. All data are interpolated into the 20CR 2.0° × 2.0° horizontal grid using bilinear interpolation and 50 hPa vertical intervals from 1000 to 250 hPa using linear interpolation, prior to the analysis.

Figure 2c–d shows the model generated internal variations over the Pacific and the Atlantic ocean (based on ALL simulations), indicating that the MMM based on 21 realizations applied in this study is capable of separating the externally forced climate responses from the model generated internal variation.

The model additivity is also tested (Fig. 2e–f) using global mean surface temperature (GMST), and linear addition of single forcing results agrees well with ALL from 1930 to 2020. However, the combined response shows a slight warming bias after the 1970s compared to ALL. Such bias can be due to (1) non-linear response when adding the separate forced response together, and (2) more importantly, the limited realization of OZ simulation (4

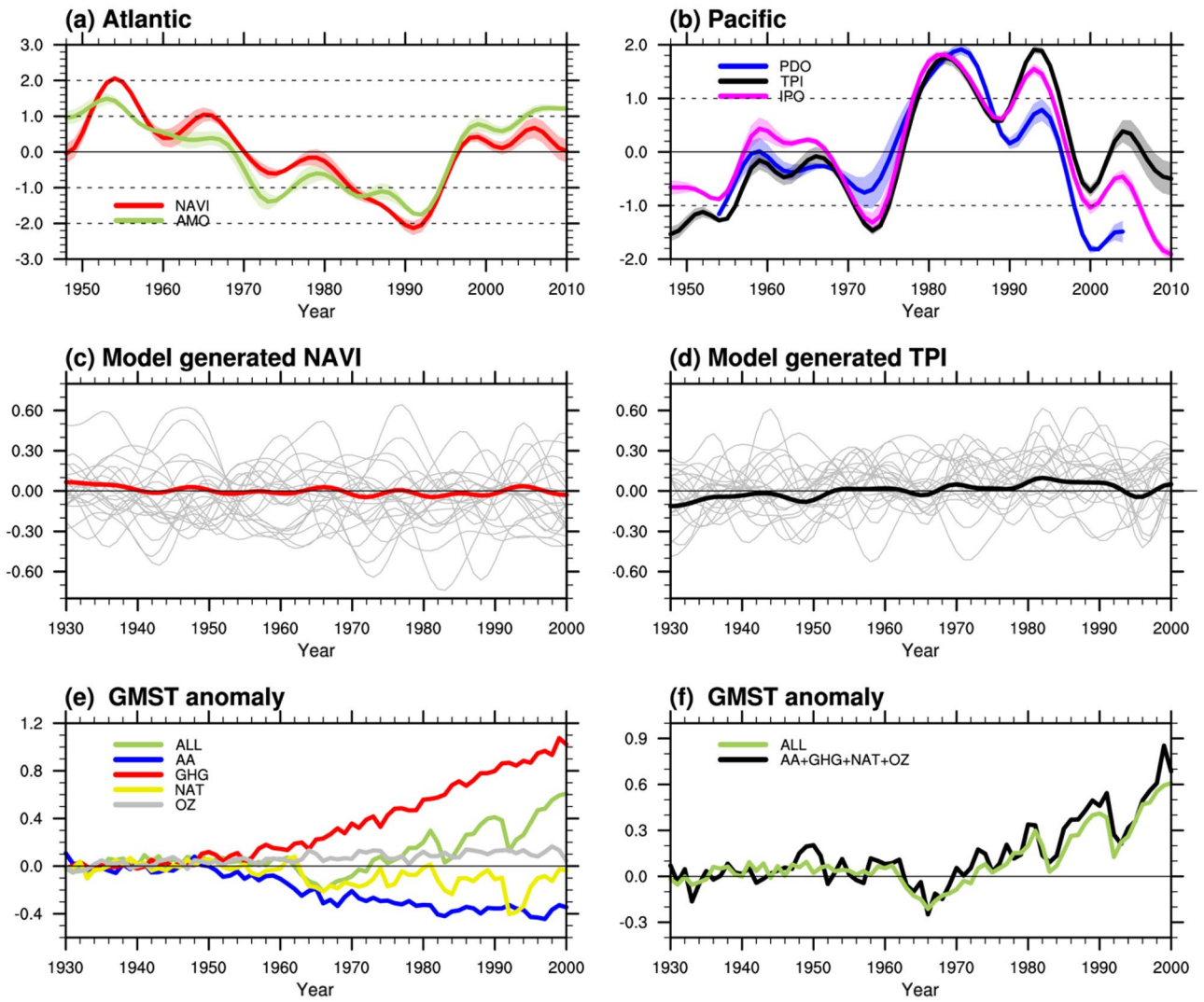

Fig. 2 **a** The time series of standardized (red) NAVI and (green) AMO index calculated from three reanalysis datasets. A 13-year low pass filter is applied to all indices. Color shadings indicate the reanalysis dataset spread. The NAVI and AMO regions are highlighted with the black boxes in Fig. 6c. **b** Similar to **a** but for standardized (blue) PDO, (magenta) IPO, and (black) TPI index. The regions for TPI definition are highlighted with the black boxes in Fig. 6a. PDO and IPO calculation is based on principal component analysis of sea surface temperature. **c**, **d** The model generated **c** NAVI index and **d** TPI index calculated from the 21 realizations of ALL simulations (grey lines) and calculated from the multi-model-mean results (red and black lines). The NAVI and TPI indices in **c** and **d** are not standardized. **e** The global mean surface temperature anomalies (GMST; K) relative to the 1930–1940 average temperature, from (green) ALL, (blue) AA, (red) GHG, (yellow) NAT, and (grey) OZ multi-model-mean results. Each experiment includes 21 realizations except for OZ, which contains 12 realizations. **f** Similar to **e** but comparing (green) ALL with the combination of the other four single forcing simulations in **e**

models and 12 realizations for OZ; 7 models and 21 realizations for the other simulations).

2.3 Internal variability in the models

To compare the relative contributions of internal variability and external forcing, we need to identify the strength of decadal variability in each model. Because each PI experiment is a long simulation run with "zero" external forcing, we use PI experiments to extract the fingerprints of decadal variability.

Several studies have shown that Pacific and Atlantic variability have strong interconnections (Wu et al. 2011; Chylek et al. 2014; McGregor et al. 2014). Although Pacific and Atlantic variability are correlated, the fingerprints of the two, regardless of their origins, are very different. Here we aim to attribute the observed asymmetric air temperature trend to the unique fingerprints of external and internal drivers, without probing into the deeper issue of interconnection between these drivers (e.g., Pacific vs. Atlantic, or co-emission of GHGs and AA from fossil fuel sources, or the possible exciting/triggering of internal modes due to

external forcing particularly AA). Thus, we treat the Pacific variability and the Atlantic variability as two independent driving factors to study their contributions to the observed trend. However, we also consider a fingerprint of the overall Decadal Variability ("overall DV") in our attribution methods, which considers the Pacific and Atlantic variability simultaneously (details of definition in Sect. 4.3).

Many studies represent Pacific variability in terms of IPO or Pacific Decadal Oscillation (PDO) (e.g., Mantua and Hare 2002; Schneider and Cornuelle 2005; Meehl et al. 2009, 2013a; Dong and Dai 2015; Newman et al. 2016). The IPO index is calculated based on the Empirical Orthogonal Function (EOF) analysis of the Pacific sea surface temperature (SST). The PDO index is similar to IPO but only uses the North Pacific SST for EOF analysis. Here we use the "Tripole Index (TPI) for the IPO" introduced by Henley et al. (2015), with a much simpler calculation. TPI is calculated using averaged SST anomaly over three regions (region 1: 25° N–45° N, 140° E–145° W (northern Pacific); Region 2: 10° S–10° N, 170° E–90° W (eastern tropical Pacific); Region 3: 50° S–15° S, 150° E–160° W (western southern Pacific)). Specifically, TPI = SST2 − (SST1 + SST3)/2. TPI has been shown to be a robust representation of IPO with a very high temporal correlation (Henley et al. 2015; Yao et al. 2021; comparison shown in the right panel of Fig. 2). Also, we apply a 13-year low-pass filter to TPI to smooth out short-term variability such as ENSO.

We represent the Atlantic-based variability using an index called North Atlantic Variability Index (NAVI), which is defined as the averaged SST anomaly in the North Atlantic basin (40°–60° N, 15°–50° W) minus the Northern Hemisphere mean anomaly (Haustein et al. 2019). NAVI is different from the widely used metric of Atlantic Multidecadal Variability (AMV or AMO; Schlesinger and Ramankutty 1994), which is normally defined as the North Atlantic SST anomaly minus the global mean SST (comparison shown in the left panel of Fig. 2). Adopting NAVI as the primary metric as suggested in Haustein et al. (2019), instead of AMO/AMV, is motivated by previous studies (e.g., Booth et al. 2012) showing AMO/AMV can be influenced by external forcings (notably European aerosols). We tested both NAVI and the traditional AMV index (subtracting global mean SST from the Atlantic SST) in our attribution analysis, and our results show that, for the most part, NAVI and AMV show similar fractional variances. A 13-year low-pass filter is also applied to NAVI.

Note that the decadal variability in the model runs does not have the same phases as in the observations during the mid-20C because the coupled models randomly generate oceanic variations while reanalysis datasets are constrained to match observed oceanic variation. To quantify how decadal variability can potentially affect the observed temperature trend, we use the negative/positive trend of TPI/NAVI to extract the individual fingerprints from the Pacific and Atlantic: we calculate the 31-year linear trend of TPI/NAVI based on the 300-year PI runs from each model and pick three separate (i.e., non-overlapping) periods with the largest negative/positive trends. We collect three samples for each model here to match the number of model runs in ALL, GHG, and AA experiments.

In addition to TPI and NAVI, we also pick samples from PI runs to represent the "overall DV" based on the temporal similarity between PI and reanalysis results: We first calculated the temporal correlation coefficients (at least 0.35 to meet the 95% significance level) between the simulated TPI/NAVI time series and that in reanalysis mean results during 1948–1978, and then pick three 31-year periods from each model that have the highest average value of TPI correlations and NAVI correlations.

3 Observed trends of tropospheric temperature in the mid-twentieth century

3.1 The slowdown of global warming

Figure 1a and b show the time series of concentrations of major GHGs and major anthropogenic aerosol emission categories, and Fig. 1c shows the global mean surface temperature from 1940 to 1980. GHG concentrations continuously increased during these four decades, which should have provided a positive forcing to the Earth system and driven a warming trend. While on the other hand, several natural or anthropogenic forcings such as volcanic eruption and anthropogenic aerosol emission contribute to the cooling tendency. The surface air temperature during 1940–1980 remained in a stable or even slightly cooling state, with little or no apparent warming in all four reanalysis datasets. The average warming trend is 0.03 K/decade from 1948 to 1978 (straight lines in Fig. 1c), which is much smaller than the significant warming during the 30 years of 1990–2019 at about 0.2 K/decade.

Despite different coverage lengths and assimilation schemes (Table 1), all three reanalysis datasets agree well after 1950 for the surface air temperature (Fig. 1c). However, there are some disagreements between 20CR and CERA20C in the surface air temperature before 1950 (not covered by NCEPNCAR and JRA55). 20CR (blue) has a larger variation compared to CERA20C (red) in this period, especially from 1944 to 1952. This stronger fluctuation is the reason for the larger 30-year linear trend (with an earlier starting year between 1945 and 1950) in 20CR (at about 0.07 K/decade) than the other two datasets. 20CR has the longest record (starting in 1850), but it only assimilates synoptic pressure, SST, and sea ice distribution, which could all be quite uncertain before the end of WWII (1945). Encouraged

by the overall good agreement of the three datasets after 1948 (and of all four datasets including JRA-55 after 1958), in the following analysis, we will consider the *average* of all three reanalysis datasets as a depiction of the mid-20C warming slowdown (Table 3).

It is also worth noting that two major volcanic eruptions (marked as the blue dashed vertical lines in Fig. 1c) are associated with a rapid decrease of temperature for about 1–2 years, but not a decadal temperature trend. This is consistent with what we show in Sect. 2.2.

Figure 1c and d justify 1948–1978 as our choice of the slowdown period because NCEPNCAR (green) and CERA20 (red) show nearly identical linear trends for the 31-year period starting between 1955 and 1958, with a negligible trend around 0 to 0.05 K/decade starting in 1948. In terms of the decadal temperature trend (K/decade shown in Fig. 1d), NCEPNCAR (green) is only slightly larger than that in CERA20C (red) during the 1948–1978 period. The larger temperature trend as in 20CR (about 0.07 K/decade) is again largely affected by the data inconsistency from 1945 to 1950, but not statistically distinct from the trend computed from the other two datasets, which is illustrated by the overlap of uncertainty ranges (color shadings) of Fig. 1d.

A fresh perspective of this study is to investigate tropospheric temperature as a whole to understand the decadal trend in the mid-20C. Figure 1e shows global mean air temperature changes at 500 hPa, which experienced a similar slowdown during the mid-20C but with a larger short-term variance. The inconsistency of 20CR (blue shading in Fig. 1e) with other datasets before 1950 is more apparent than the surface temperature (in Fig. 1c), but again, all four datasets agree well after the 1950s.

3.2 Latitudinal asymmetry

3.2.1 Horizontal perspective

As in Fig. 1, both at the surface and in the mid-troposphere, all datasets show a robust global "cooling" during the mid-20C, despite growing GHG forcing. However, global warming or cooling is not spatially uniform, so we show the near-global (60° S–60° N) patterns of the decadal temperature trend during the mid-20C in Fig. 3.

Spatial patterns of the 31-year linear trends of the surface air temperature over the ocean are shown in Fig. 3a, c, and e, for the three datasets. Focusing on the low and mid-latitude ocean, all three datasets agree well in the Pacific and the Atlantic Oceans, with cooling in the northern Pacific and Atlantic and warming in the Southern oceans. The cooling-warming contrast from the north to the south Atlantic Ocean is evident in all three datasets. This pattern is similar to the typical pattern of a negative NAVI phase, indicative of the potential role of Atlantic variability during this period, which we will quantitatively test later.

Figure 3g shows the zonal mean temperature trend (ZMTT) near the surface during the 1948–1978 period. Some differences exist in low latitude regions, where NCEPNCAR (green) shows warming of 0.15 K/decade over the oceans, while ZMTT in 20CR and CERA20C is within ± 0.05 K/decade. Nevertheless, a strong latitudinal gradient is evident in all three datasets with continued Southern Hemisphere (SH) warming (0.1–0.2 K/decade) but moderate Northern Hemisphere (NH) cooling (0.05–0.2 K/decades), which amounts to − 0.3 to − 0.2 K/decade/90° Lat.

Figure 3b, d, and f (the right column) show the mid-tropospheric (500 hPa) spatial patterns of 1948–1978 temperature trends, which are smoother than, and about twice as strong as at the surface. Spatially, major parts of NH show cooling trends, while most of the SH mid-latitude regions beyond 30° S show significantly warming trends. The strongest cooling occurs over eastern North America and from the northern Atlantic across Europe to the northern Pacific. Over Asia, CERA20C and NCEPNCAR show similar (with pattern correlation as high as 0.70) spatial patterns with strong cooling over major parts of East Asia, while the 20CR dataset, in contrast, shows warming over northern Asia.

In Fig. 3h, the latitudinal asymmetries at 500 hPa are also smoother, with gradients about twice as large as the surface (note the y-axis difference in Fig. 3 g and h). Despite the spatial differences among the three datasets, the ZMTT (Fig. 3h) features the cooling-north/warming-south gradient consistently in all three datasets, with the strongest cooling (warming) at 30°–50° N (°S) and a close-to-zero trend over the tropical regions.

Table 3 2-D spatial pattern correlation coefficients of temperature trends (as in Fig. 3a–f) at different pressure levels, between each two of the three reanalysis datasets (CERA20C, NCEPNCAR, and 20CR)

Pressure level (hPa)	CERA20C vs. 20CR	NCEPNCAR vs. 20CR	CERA20C vs. NCEPNCAR	Mean of the three columns to the left
300	− 0.30	− 0.01	0.83	0.17
400	0.23	0.36	0.73	0.44
500	0.31	0.44	0.70	0.49
600	0.29	0.65	0.57	0.50
700	0.29	0.39	0.64	0.44
800	0.31	0.18	0.63	0.37

3.2.2 Vertical perspective

The latitudinal gradient of ZMTT (K/decade/90° Lat) is a key metric we will use for attribution, which sets this study apart from many previous ones. In Fig. 4, we focus on the latitudinal asymmetry of ZMTT at 500 hPa because it is largely representative of the free troposphere. Here,

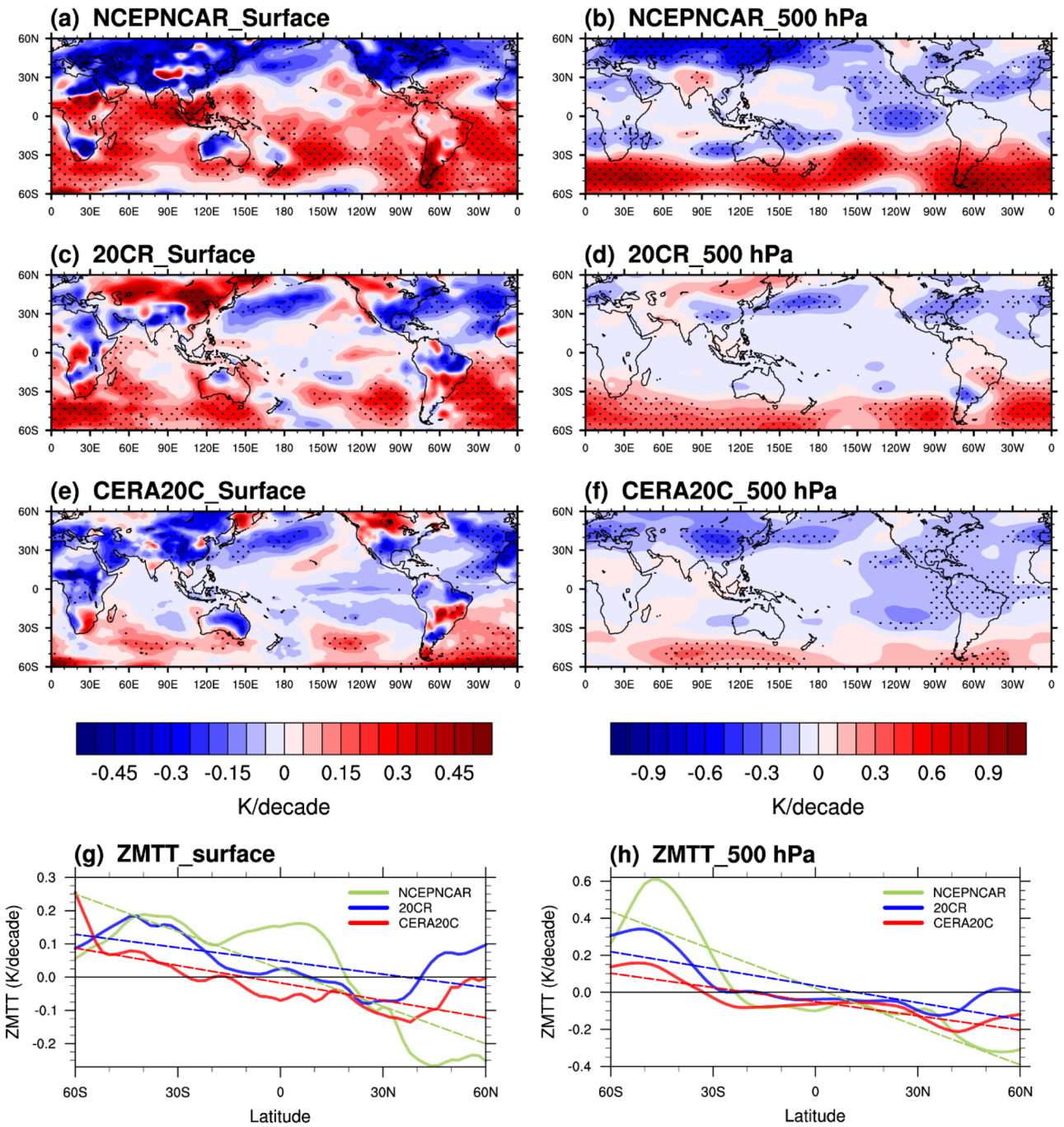

Fig. 3 **a**–**f** The spatial patterns (60° S–60° N) of the 31-year linear trend of air temperature during 1948–1978 at the surface (**a**, **c**, **e**), and at the 500 hPa level (**b**, **d**, **f**) from NCEPNCAR (row 1), 20CR (row 2), and CERA20C (row 3). The black dots show regions where the local trend passes the 95% significance t-test. **g**, **h** The solid lines are zonal mean temperature trends (ZMTT) derived from the spatial patterns in **a**–**f**. The colored dashed lines are linear fits of ZMTT, depicting the latitudinal (i.e., meridional or north–south) gradient. Note that the color scales and y-axes are different between the left and the right panels, with the 500 hPa level featuring larger trends and a stronger latitudinal gradient

we further examine the latitudinal asymmetry in the entire troposphere from 1000 to 250 hPa.

Figure 4a–c shows that the latitudinal asymmetry is persistent in all levels of the lower and middle troposphere in all three reanalysis datasets, with significant warming from 30° S to 60° S and cooling beyond 30° N. In NCEPNCAR and CERA20C, significant warming also occurs over the tropical and subtropical lower troposphere. Significant

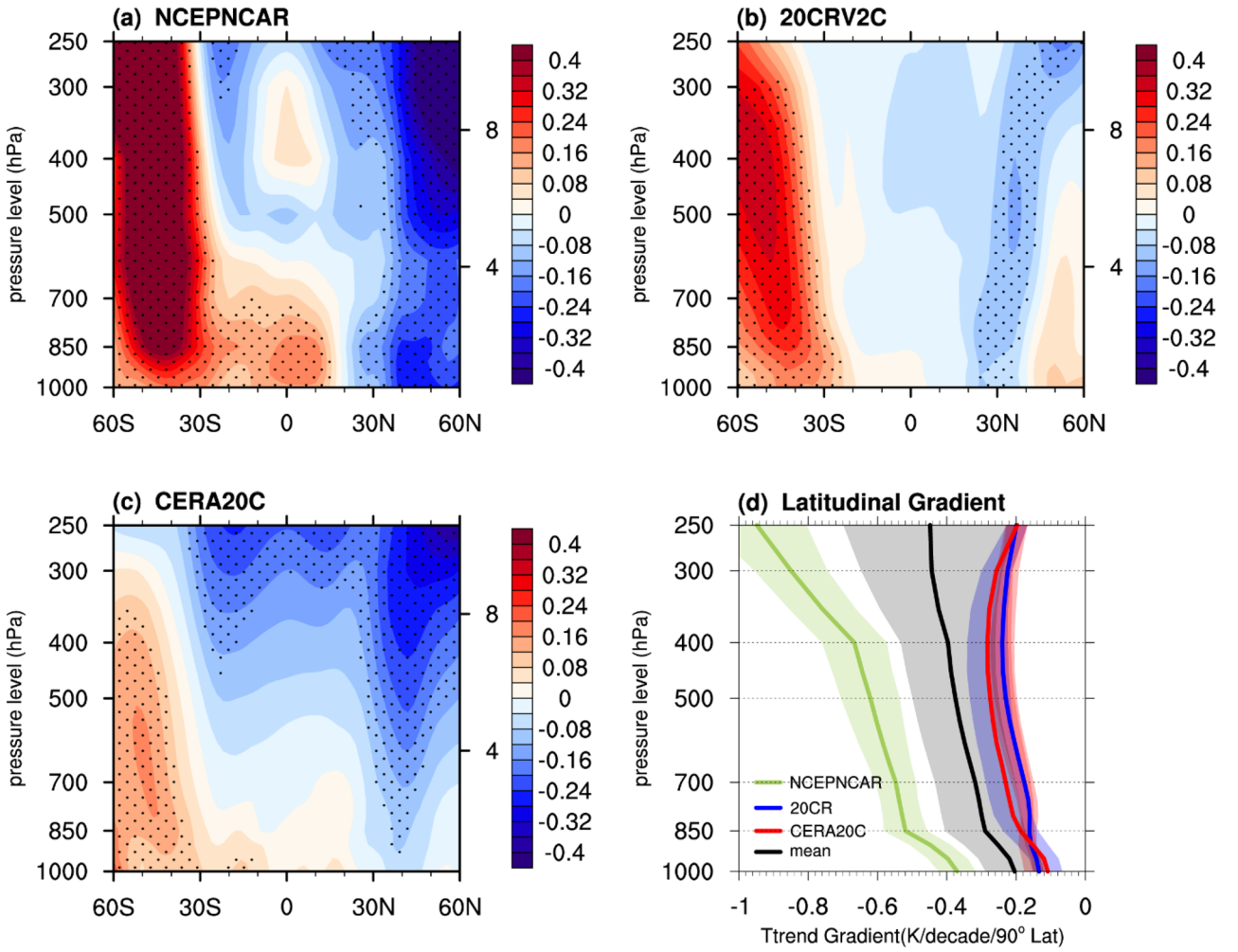

Fig. 4 **a**–**c** The vertical patterns of ZMTT from 1948 to 1978 from three reanalysis datasets. The black dotted areas pass the 95% significance test. **d** The latitudinal gradients of the zonal mean temperature trends (ZMTT, in K/decade/90° lat). The green, blue and red shadings show the 95% confidence interval of linear regression from the three reanalysis datasets. The black line shows the average of the three datasets, and the grey shading represents the standard errors

cooling in NCEPNCAR and CERA20C occurs over NH mid-latitudes and then expands to tropical and subtropical middle and upper troposphere. In comparison, 20CR does not show significant warming or cooling over tropical and subtropical regions throughout the troposphere. The drastic shift from south-warming to north-cooling over the mid- and low-latitude regions indicates that external forcing could be another key factor, in addition to decadal variability, contributing to the latitudinal asymmetry by directly affecting the radiation budget of the mid-troposphere. This will be quantitatively assessed in Sect. 5.

In Fig. 4d, the latitudinal gradients are shown as a function height. It is significantly negative in all three reanalysis datasets. However, the latitudinal gradient shrinks above the 400 hPa level in CERA20C (blue) and 20CR (red) while it continues to strengthen in NCEPNCAR (green). Also notably, the latitudinal gradient in NCEPNCAR is two to three times larger than the other two datasets even at the surface level, consistent with the vertical pattern shown in Fig. 4a, where NCEPNCAR has significant warming in the SH at all pressure levels, compared with the muted warming beyond 400 hPa in the other two datasets. Previous studies have pointed out the potential bias problems of NCEPNCAR, especially during the pre-satellite era. 20CR is also questioned by some studies by only assimilating the surface observations. We conducted detailed robustness tests on the three reanalysis datasets (see Sect. 1 of the supplementary document) and found that the latitudinal asymmetry we discussed here is robust among the three datasets. Therefore, for the following analysis, we consider the average of these three datasets (black line in Fig. 4d) as the observational benchmark

(Reanalysis Mean, "RE"') for the attribution, with the uncertainty (grey shading in Fig. 4d) well-considered.

4 Simulated trends of tropospheric temperature in the mid-twentieth century

4.1 Latitudinal asymmetry

This Section quantifies potential contributors to the latitudinal asymmetric temperature trends using the Global Climate Model (GCM) outputs. First, we compare the Reanalysis Mean (RE, the average of the three main reanalysis datasets) results with the Multi-Model Mean (MMM) of All-forcing experiments (ALL, seven models with a total of 21 runs) to verify whether the model can reproduce the observed asymmetry pattern.

Figure 5a–d shows the spatial patterns of the 1948–1978 temperature trend at the surface and 500 hPa levels from RE and ALL. At the surface (left column), the latitudinal asymmetry of temperature trends is largely consistent except for the tropical regions, where ALL shows a cooling tropical Pacific, but RE does not show a significant trend.

Note that the RE and ALL patterns have different color scales since the magnitude of the RE trend is about twice as large as for ALL. The ALL patterns are the average of 21 ensemble members from seven models with randomly generated decadal variability, which means the decadal variability contribution is smoothed out in the ensemble average results. On the other hand, RE is the average of three reanalysis datasets with the same "real-world" decadal variability. Therefore, it is reasonable that RE has larger magnitudes compared with ALL (because of the "real-world" decadal variability). Although we cannot directly compare the magnitude of RE and ALL, it is still useful to conduct comparisons based on the spatial pattern. The striking similarity as identified in Fig. 5a and c suggest the role of external forcing in causing the observed trend.

The similarity also exists for the mid-troposphere. The 500 hPa patterns are also smoother than the surface pattern, and the pattern correlation between ALL and RE is as high as 0.80. Both ALL and RE feature an overall cooling trend over the northern part starting from about 30° S and a warming trend over SH mid-latitudes (40° S to 60° S). The notable difference is that the ALL pattern (Fig. 5d) does not have much zonal (i.e., east–west) variation, especially over the Pacific, compared to the RE pattern, again likely due to the smoothing of decadal variability in ALL model results.

As mentioned in the Introduction and Sect. 3, the latitudinal asymmetry of ZMTT is a key indicator to quantify contributions to the mid-20C slowdown. Figure 5g and h show the ZMTT as a function of latitude. While some pieces of evidence show that the latitudinal asymmetry could be caused by decadal variability, the ALL pattern still carries strong latitudinal asymmetry even with decadal variability smoothed out by the ensemble averaging. Therefore, the ALL-RE similarity (black and green) leads us to hypothesize the potential role of external forcing.

The next two subsections (Sects. 4.2 and 4.3) extract the fingerprints of various external forcings (GHG and AA) and internal decadal variability originating from different ocean basins (TPI and NAVI).

4.2 The fingerprints of external forcings

To isolate the fingerprints of different external forcings, we examine seven CMIP5 models, each with three sets of experiments introduced in Sect. 2.3: ALL, GHG, and AA. Since each model contributes three realizations for each experiment, the MMM results are the average of 21 runs in total, and thus the randomly distributed decadal variability in each sample is largely smoothed out. As a result, the MMM temperature trends during mid-20C from ALL, GHG, and AA only contain the climate responses to those external forcings. Figure 5c and d show the surface and 500 hPa spatial patterns from ALL. Figure 6b, d, and e show the 500 hPa spatial patterns from each single forcing. Figure S3 in the supplementary document shows surface patterns from the single forcing experiments.

To examine whether a set of 21 realizations is large enough to rule out the contribution of natural variability to the MMM results, we calculate the TPI index and NAVI index from MMM results and compare that with the indices from individual realizations. We find that MMM results contain little variations of TPI and NAVI compared with the magnitude of individual realizations (Fig. 2c–d). This indicates that the 21-member mean here is capable of effectively separating externally forced responses from the model-generated internal variations in decadal to multi-decadal time scales.

4.3 The fingerprints of decadal variability

There is a challenge to identify the fingerprints of decadal variability because their phases are randomly distributed in model runs. As mentioned in Sect. 2.3, we used the "similarity" method to identify the overall DV, and the rationale is to reproduce the real-world overall DV patterns ("DV" in Fig. 5e and f) just as the historical external forcings introduced in other single forcing experiments.

In addition to the overall DV, the 500 hPa patterns of TPI and NAVI are shown in Fig. 6a and c, which are picked based on the "negative trend" method (see Fig. S3 in the

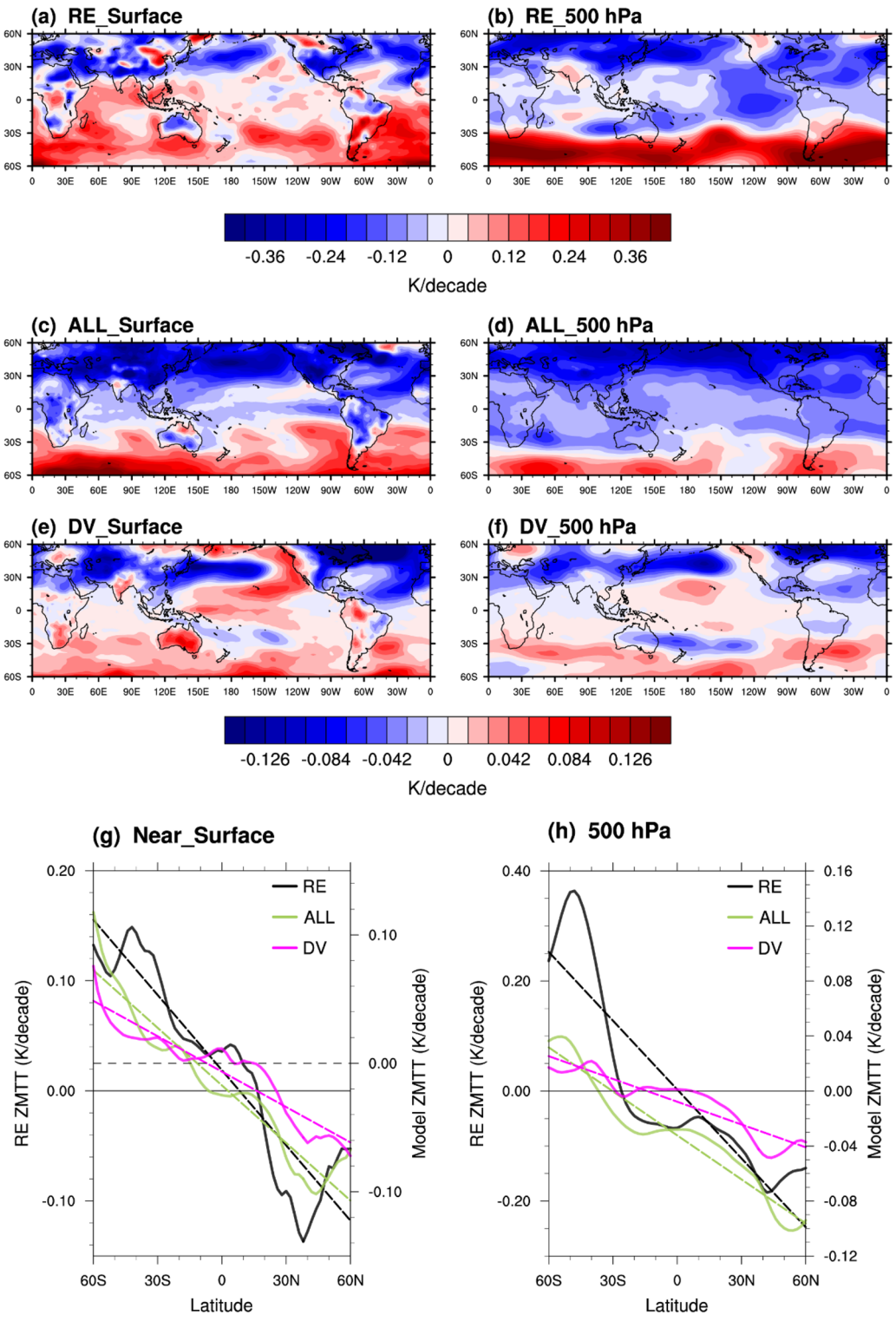

Fig. 5 **a**–**f** Spatial patterns (60° S–60° N) of the 31-year (1948–1978) linear trend of air temperature (K/decade) at the surface (left) and 500 hPa (right) based on **a**, **b** the reanalysis mean (RE), **c**, **d** all-forcing simulation (ALL), and **e**, **f** decadal variability (DV) derived from the model's PI control simulation. Note that the color scales for **a** and **b** differ from that for **c**–**f**. **g**, **h** The zonal mean temperature trend (ZMTT, K/decade). Similar to Fig. 3g and h but contrasting RE, ALL, and DV. Note that the left and right vertical axis values in **g** and **h** differ too

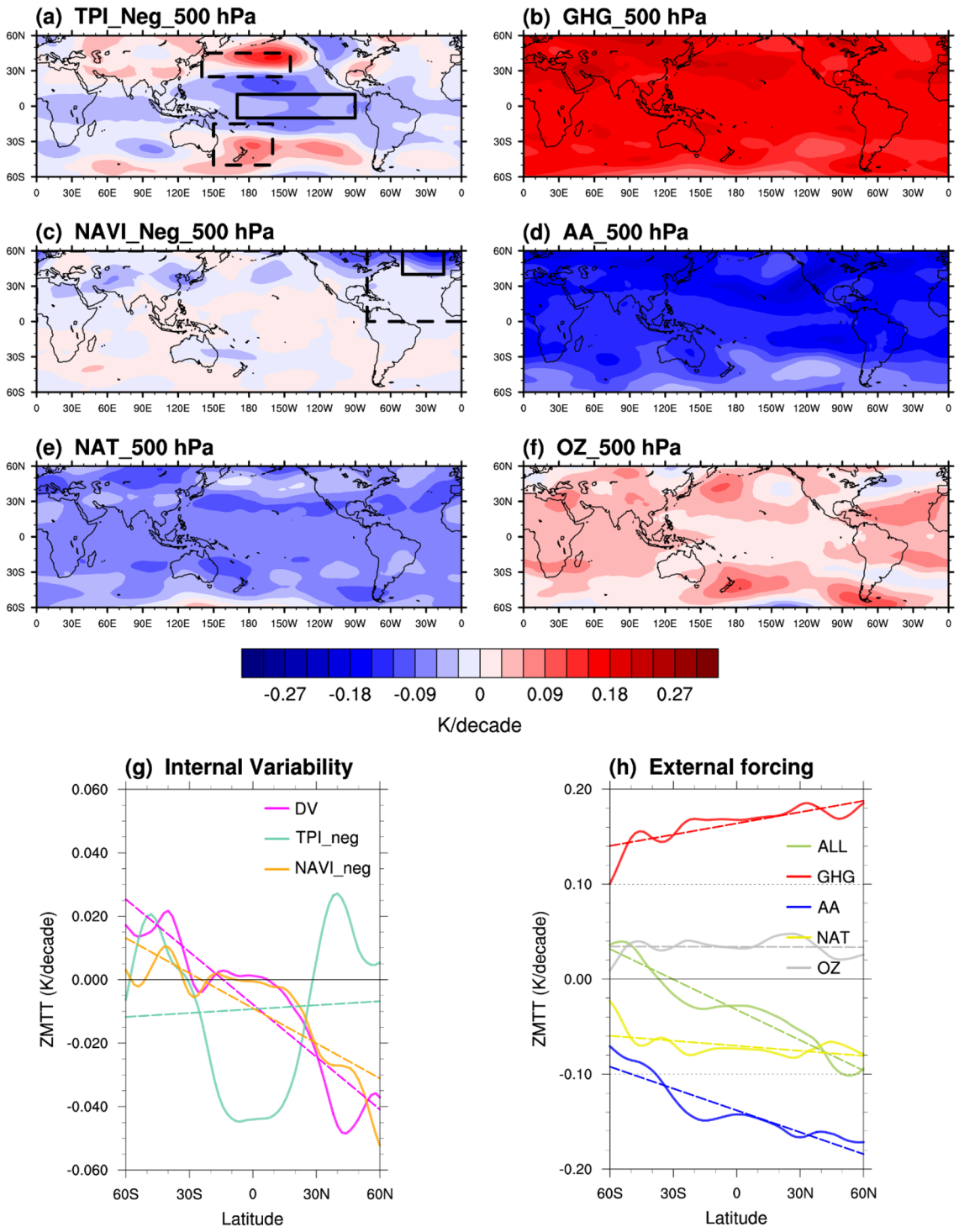

Fig. 6 **a**–**f** Spatial patterns (60° S–60° N) of the 31-year linear trend of air temperature during 1948–1978 at 500 hPa. **a** and **c** show patterns due to internal variability calculated from Pre-Industrial (PI) model runs. **a** TPI is defined using a negative trend, and **c** NAVI is defined using a negative trend. The **b**, **d**, **e**, **f** shows the patterns due to external forcing. **b** GHG-only, **d** aerosol-only (AA), **e** natural-forcing-only (NAT), and **f** ozone-only (OZ). **g** The ZMTT induced by internal variability, and **h** ZMTT induced by external forcings. The TPI regions are highlighted with the black boxes in **a**; The NAVI (AMO) region is highlighted with the black box using solid (dashed) lines in **c**

supplementary document for the surface patterns of TPI and NAVI). There are debates about whether the negative (or positive) *phases* or the *transitions* from positive phase to negative (or negative to positive) of these variability indices drive the decadal climate change. Our test suggests that the *transition* of NAVI/TPI is the key driver that leads the global SST pattern to *change*. In contrast, when NAVI/TPI stays in a negative (or positive) *phase*, the temperature trend remains quite small globally, but the 31-year-mean temperature *anomalies* reveal the typical patterns of NAVI/TPI, which is not relevant to the problem we set out to address in this study.

In summary, we conclude that the multi-decadal scale temperature trend is strongly tied to the *transitions* of NAVI/TPI rather than the *phases*, and thus we choose the "negative transition" samples as the Pacific and Atlantic variability fingerprints in our attribution analysis (shown as "TPI_neg" & "NAVI_neg" in Fig. 6a and c). The reason we choose negative trends is that during the mid-20C, NAVI had a negative trend (reaching the minimum around 1975), and TPI just entered a negative phase after a negative trend (a negative TPI trend started around 1940 and TPI index stayed in negative phase until 1978).

5 Attribution of the latitudinal asymmetry in tropospheric temperature trend

We now have two sets of fingerprints corresponding to both external forcings [ALL (Fig. 5c and d), GHG (Fig. 6b), and AA (Fig. 6d)] and internal variabilities [DV (Fig. 5e–f), TPI (Fig. 6a), and NAVI (Fig. 6c)]. Since ALL and DV are overall fingerprints of all kinds of external forcings and internal variability, our attribution follows two frameworks to identify separate components of ALL and DV (illustrated in Fig. 7).

- The 2-step framework compares RE with these two fingerprints (ALL and DV) first and then further quantifies the fractional variance of individual components (GHG/AA, TPI/NAVI) to the ALL and DV, respectively.

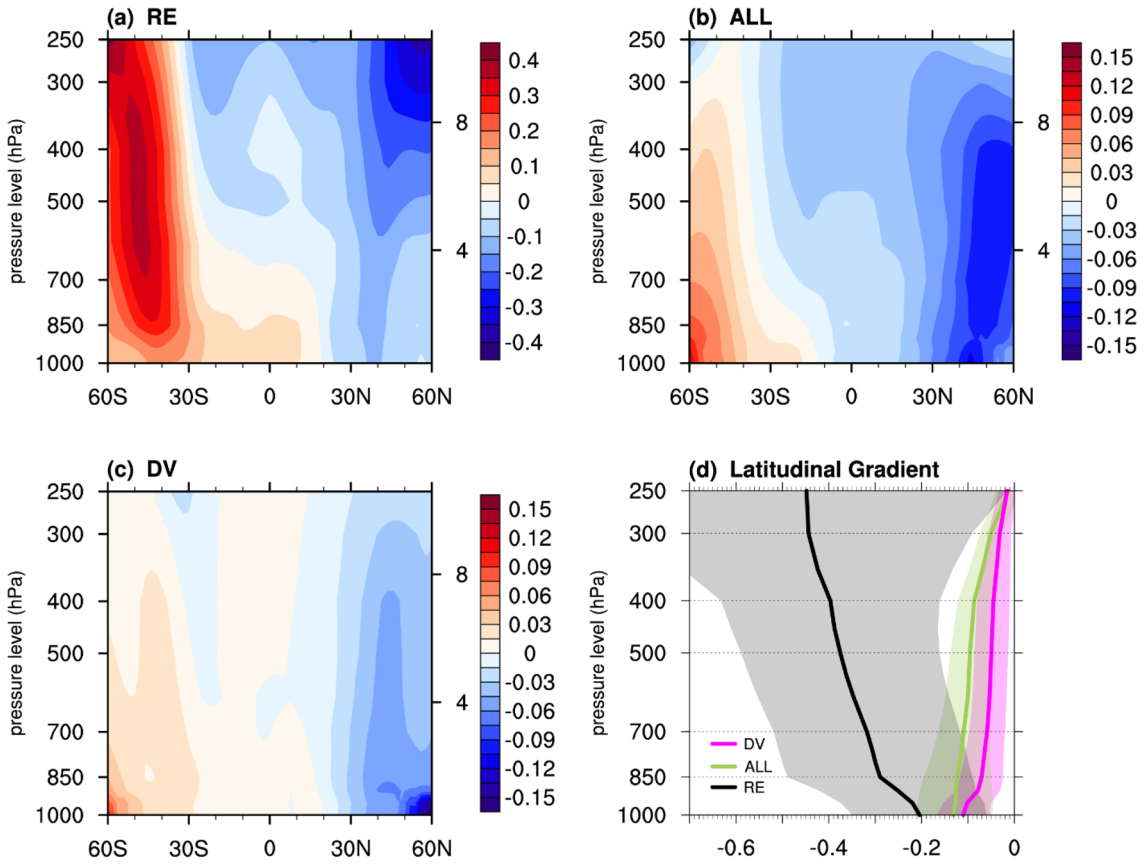

Fig. 7 Similar to Fig. 4 but showing the vertical patterns of ZMTT (K/decade) in **a** RE, **b** ALL, and **c** DV. **d** The latitudinal gradient of ZMTT (K/decade/90° Lat). The green and purple shadings represent the standard deviations of model-to-model differences from ALL and DV, and the grey shading represents the standard errors of RE (same as Fig. 4)

- The 1-step framework directly quantifies the fractional variance of the four individual components (GHG, AA, TPI, and NAVI) to the total RE pattern.

To further enhance the robustness of the results, the attribution of the observed latitudinal asymmetry and the quantification of fractional variances of each component will be based on three different aspects (horizontal pattern, vertical structure, and magnitude of trends), as discussed in the following three subsections.

5.1 Attribution based on the horizontal pattern

The 2-step attribution framework is based on the spatial patterns of the 31-year temperature trend shown in Figs. 5a–f and 6a–d. Section 4.2 already compares RE and ALL near the surface and at 500 hPa in detail and shows high correlations between RE and ALL. Here we focus on RE and DV results. DV and RE share similar spatial patterns at the surface (Fig. 5a and e), both showing cooling in the NH mid-to-high latitudes and warming in SH. However, DV induces a PDO-like warming pattern over the tropical Pacific, which is not obvious in RE. Besides, the warming over the Indian Ocean in RE is not captured in the DV pattern. At 500 hPa, DV shows slight warming over the tropics, which is different from RE and ALL, leading to a smaller pattern correlation with RE (0.46 with DV vs. 0.80 with ALL).

Based on the linear regression, we utilize the explained variance (square of the spatial pattern correlation (R^2)) to compare the relative importance of each component to the fingerprint in RE. ALL explains around 64% of the RE variance (the explained variance of each component is square of the spatial pattern correlation (R^2) of that component), while DV can only explain 21% of the RE variance (yellow entries in Table 4a). Therefore, compared with DV, ALL (the total of external forcing) contributes much stronger to the observed spatial pattern of the 500 hPa temperature trend. In contrast, at surface level (Table 4b), DV explains 14% of the RE variance while ALL explains a slightly higher (22%), which indicates that the external forcing fingerprint plays a more important role in the mid-troposphere compared with the surface.

After estimating the contributions of DV and ALL, we further explore how individual external forcings (GHG and AA) contribute to ALL, and similarly, how the Pacific (TPI) and the Atlantic (NAVI) contribute to DV (green entries in Table 4). Because of the smoother pattern and stronger similarity between RE and ALL, we focus on the mid-troposphere (500 hPa) as opposed to the surface.

For external forcings (Fig. 6b and d), AA shows a global cooling trend during the mid-20C with a stronger NH cooling (blue line in Fig. 6h, −0.069 K/decade/90° Lat), which is similar to the latitudinal gradient of the trend in ALL (green line, −0.096 K/decade/90° Lat). In contrast, the GHG pattern is global warming with an opposite latitudinal gradient (0.036 K/decade/90° Lat), featuring a stronger NH warming. Based on pattern correlations, GHG explains −26% variance fraction to the fingerprint of ALL, and AA explains 52% of the ALL variance (green entries in Table 4a).

For internal variabilities (Fig. 6a and c), the TPI fingerprint shows a nearly symmetric pattern with a

Table 4 The variance fractions explained by various internal and external factors to the observed (RE) or simulated (DV and ALL) 31-year temperature trends during the mid-20C. **a** and **b** are calculated based on the pattern correlations of the 2-D *horizontal* patterns. "Fingerprints" from individual drivers and observational "benchmarks" are shown in Figs. 5 and 6, for 500 hPa and surface (land and ocean), respectively. See Table S1 in the supplementary for ocean only results. **c** is calculated based on the pattern correlations of the 2-D *vertical* patterns. "Fingerprints" and "benchmarks" are shown in Fig. 7. The orange entries show the contributions following the 1-step framework depicted in Fig. 10a right panel, while the yellow and green entries show the contributions following the 2-step framework depicted in Fig. 10a left panel

(a) Attribution based on 500 hPa 2-D Correlation

	From DV	ALL	TPI	NAVI (AMO)	GHG	AA	NAT	OZ
To RE	21%	64%	1%	8% (22%)	-26%	55%	11%	0%
DV	-	33%	-18%	57% (61%)	-	-	-	-
ALL	-	-	-	-	-26%	52%	8%	0%

(b) Attribution based on surface (land and ocean) 2-D Correlation

	From DV	ALL	TPI	NAVI (AMO)	GHG	AA	NAT	OZ
To RE	14%	22%	0%	16% (21%)	-7%	20%	4%	0%
DV	-	-	-14%	63% (63%)	-	-	-	-
ALL	-	-	-	-	-13%	28%	7%	1%

(c) Attribution based on vertical 2-D Correlation

	From DV	ALL	TPI	NAVI (AMO)	GHG	AA	NAT	OZ
To RE	42%	62%	2%	25% (46%)	-32%	55%	24%	-3%
DV	-	-	-13%	83% (79%)	-	-	-	-
ALL	-	-	-	-	-33%	61%	34%	1%

positive–negative-positive pattern from south to north, which is obviously different from the overall DV fingerprint. Indeed, the fractional variance explained by TPI to overall DV is -18% (green entries in Table 4a). In contrast, the NAVI fingerprint resembles the latitudinal asymmetry in DV (Fig. 5e) and the temperature trends over most regions globally, notably strong cooling over the North Atlantic and moderate warming over SH mid-latitudes. The horizontal spatial correlations suggest that NAVI explains 57% of the DV fingerprint. Here we also compare the different roles of NAVI and AMO. The conclusion that Atlantic variability, not Pacific, contributes significantly to the observed asymmetry still holds after switching from NAVI to AMO as the metric, and AMO explains slightly larger variance fractions than NAVI at 500 hPa (61 vs. 57%), and similar variance fractions at the surface (81 vs. 77%; see Table S1 in the supplementary). As is discussed in the previous study (Booth et al. 2012; Haustein et al. 2019), the AMO/AMV can be influenced by external forcings, and thus should not be treated as the pure internal variabilities in detection and attribution works.

Note that the fractional variances here do not add up to 100%, suggesting other factors can also be in play (as well as uncertainties from incomplete data and imperfect modeling). Also, contributions can be negative values since they are based on pattern correlations (i.e., the sign of the correlation is preserved). Another thing to be mentioned is the cross-correlations between each forcing (correlation between DV and ALL shown in Table 4). The ALL and DV show similar horizontal patterns, especially at 500 hPa (33%; Table 4a). It indicates the difficulty of separating the fingerprints of ALL and DV and brings uncertainties to the explained variance fractions.

However, the DV fingerprints are objectively picked (with the largest negative trend) from PI runs, where no external forcing is included. On the other hand, the fingerprints of external forcings are obtained based on the MMM results of single forcing experiments, in which the model-generated internal variabilities are largely smoothed out. By identifying fingerprints of DV and external forcings independently, we aim to mitigate the concerns of entanglement of external forcing and internal variability (especially the potential role of AA in shaping Atlantic variability) when attributing the RE patterns to different factors.

The quantitative attribution above is based on the 2-step framework, but we also test the robustness of the results using1-step framework, which is to calculate the contribution of each individual forcing by directly comparing its fingerprint with the RE pattern (summarized in the orange cells of Table 4a). The 2-step results show that the contribution of NAVI to the 500 hPa trend is one-third of that explained by DV (8% compared with 21%), while the TPI has no significant contribution to the RE pattern. For the external forcings, AA is consistently estimated to contribute more than 50% (55% in the 1-step framework; 52% in the 2-step framework) to the RE pattern regardless of the attribution framework in use.

Comparing two attribution frameworks, we find that the contributions of internal variability and external forcings to the 500 hPa pattern are similar. External forcings (primarily due to AA) have an overall larger contribution than internal variability with a weak contribution from NAVI. Not surprisingly, GHG has a negative contribution to the latitudinal gradient as its fingerprint is generally the opposite of AA. The symmetric TPI fingerprint does not provide a significant contribution to the mid-20C temperature trend pattern.

The analysis so far (as in Fig. 6) focuses on the contributions at 500 hPa, but do the results change with height? Table 4b shows that the contribution of DV at the surface is larger compared with the mid-troposphere. The contribution of DV decreases from 21% (500 hPa) to 14% (surface) with height, while the ALL contribution decreases from 64% (500 hPa) to 22% (surface), which means that ALL contributes slightly larger than DV at surface level. The contribution of NAVI to RE at the surface is larger than that at 500 hPa (16 vs. 8%). However, the contributions of AA to RE decrease significantly at the surface in comparison to 500 hPa (from 55 to 20%) but is still slightly larger than the contribution explained by NAVI (16%).

Based on the spatial pattern correlation analyses in this subsection, we conclude that both internal variability (primarily driven by NAVI) and external forcings (primarily driven by AA) play important roles in the decadal temperature trend during the mid-20C. More importantly, the relative roles of NAVI and AA vary with altitude: the explained variance of AA is similar to that of NAVI on the surface but is significantly larger in the mid-troposphere.

5.2 Attribution based on the vertical pattern

Since the contributions of internal variability and external forcings vary with altitude, we further estimate the contribution by taking advantage of the combined picture of the entire troposphere up to 250 hPa. The latitudinal asymmetry signal is persistent at all pressure levels both in ALL (Fig. 7b), which is consistent with all three Reanalysis datasets (previously shown in Fig. 4a–c, with the mean shown in Fig. 7a). Based on the vertical pattern correlation (Table 4c), ALL has a greater contribution (62%) than DV (42%).

The latitudinal asymmetry in DV only weakly occurs near the surface, and the gradient decreases monotonically with altitude (Fig. 7d). Also, DV fingerprints in SH carry no positive trends at all pressure levels (Fig. 7c), which is inconsistent with the RE. In contrast, ALL can capture the cooling trend over tropical regions in the mid-troposphere. Also, the mid-troposphere response to ALL still shows a

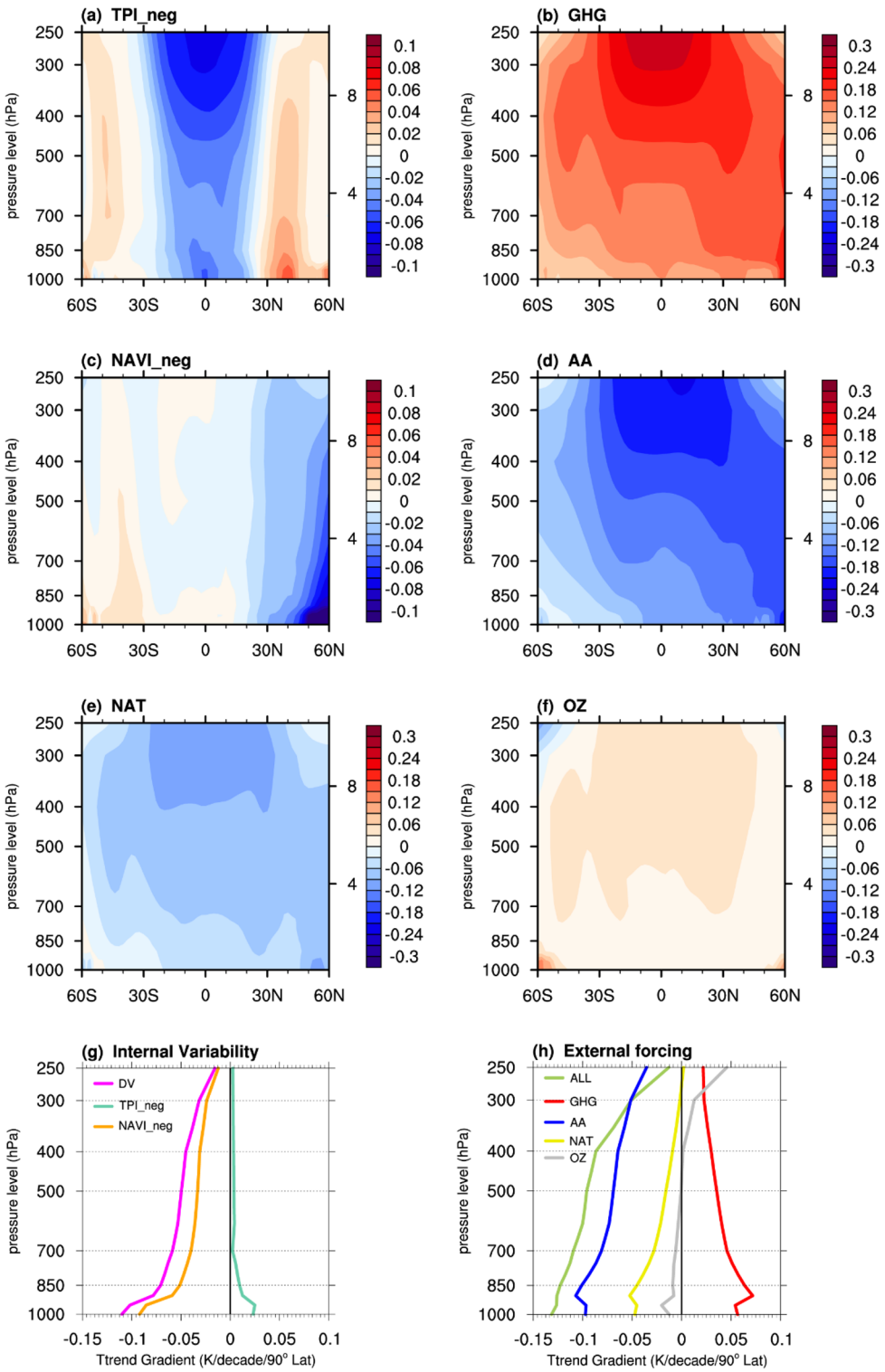

Fig. 8 Similar to Fig. 7 but showing **a**–**f** vertical patterns of ZMTT (K/decade) due to internal variability **a** TPI and **c** NAVI; and due to external forcing: **b** GHG, **d** AA, **e** NAT, and **f** OZ. **g**, **h** Vertical profiles of the latitudinal gradients of ZMTT (K/decade/90° Lat), **g** DV, TPI, and NAVI results; **h** externally forced responses

significant latitudinal gradient, despite being smaller than the near surface, which is more consistent with that in RE compared with DV. Overall, the difference between DV and ALL indicates that external forcings play more important roles in shaping the mid-tropospheric latitudinal gradient than DV, while at the same time, DV and ALL both substantially contribute to the asymmetry at the surface. This is probably because external forcings such as GHGs and aerosols can directly affect the tropospheric climate via both rapid adjustment (Smith et al. 2018) and simulations of oceanic slow feedback (e.g., Xu and Xie 2015), while the coupled ocean-atmospheric processes

giving rise to DV largely affects the climate "bottom-up" from the surface.

Next, we discuss the role of individual external and internal factors.

The temperature responses of TPI and NAVI are shown in Fig. 8a and c. TPI shows an asymmetric warming-cooling-warming pattern from south to north with significant cooling over the tropical regions, which is not consistent with RE (Fig. 7a) or DV (Fig. 7c). Therefore, TPI hardly contributes to the latitudinal asymmetry in DV (− 13% in Table 4c). In contrast, the NAVI pattern is significantly correlated to the vertical pattern of DV (with an estimated contribution of 79%) but with stronger warming over the SH and weaker cooling over the NH.

Comparing the vertical profiles between TPI and NAVI (Fig. 8g), a very similar structure and magnitude with DV (Fig. 7c) can be found in NAVI. In contrast, the TPI response has almost no latitudinal asymmetry above 700 hPa and only a weak positive gradient close to the surface, suggesting a small contribution of TPI to the mid-20C temperature trend.

As for the external forcings (Fig. 8b and d), GHG has a negative contribution of -33%, and AA contributes 61% to ALL (following the 2-step attribution framework). From the vertical profiles of different external forcings (Fig. 8h), we see a similar vertical profile of the latitudinal gradient between ALL and AA (green and blue) and the opposite gradients from GHG. Note that the gradient from AA is about two times larger than from GHG at all pressure levels, which is why AA forcing can offset the influence of GHG forcing. The comparisons based on magnitude are discussed in detail in the next subsection.

Lastly, we test the 1-step framework of directly partitioning the contributions (orange cells in Table 4c), which yields similar results as in the 2-step framework (yellow and green cells in Table 4c). Overall, AA and NAVI are the major contributors to observed patterns in RE (with a contribution of 55 and 46%, respectively), while GHG contributes − 32%. The vertical pattern approach here yields largely similar results compared to the results from the 500 hPa spatial pattern method (Table 4a), but the DV contribution increases from 21 to 42% (mainly from NAVI increasing from 22 to 46%), again emphasizing the more important roles of internal variability at lower altitudes, and less so in the mid-troposphere.

5.3 Attribution based on the magnitudes of the latitudinal gradient

The previous two subsections show that the two attribution frameworks, based on pattern correlation, yield consistent results. However, the pattern correlation alone does not consider the response magnitudes. This subsection performs the attribution based on the response magnitudes of different forcings. In the correlation-based analysis, we can directly compare RE and model results. However, here we cannot directly compare the two because of the large magnitude differences (indicated by the different color scales of Fig. 3). Instead, we focus on the magnitudes of different fingerprints in models to estimate the contributions of external forcings and internal variability from a different perspective from the previous subsections.

The gradient of ALL at 500 hPa is − 0.096 K/decade/90° Lat (green line in Fig. 5h), and the gradient of DV is − 0.050 K/decade/90° Lat (purple line in Fig. 5h). Therefore, the contribution of ALL to the observed gradient is about twice the DV contribution at 500 hPa based on response magnitude, which is consistent with the results from the previous correlation methods. The comparison between TPI and NAVI is also consistent with previous methods. At 500 hPa, compared with the NAVI gradient (orange line in Fig. 6g, − 0.033 K/decade/90° Lat), the TPI gradient is positive but is only 0.004 K/decade/90° Lat (light green line in Fig. 6g), which indicates that the ZMTT response to TPI is largely latitudinally symmetric. Thus, DV asymmetry mainly comes from the NAVI transition during this period, which contributes to about 88% of the DV asymmetry in terms of magnitude. Similarly, the latitudinal gradient due to AA is − 0.069 K/decade/90° Lat at 500 hPa (blue line in Fig. 6h), compared with 0.036 K/decade/90° Lat due to GHG (red line in Fig. 6h). Thus, in terms of ZMTT gradient magnitudes, AA explains about 72% of the asymmetry in ALL.

As we previously argued, external forcings can be more important compared to internal variability in the mid-troposphere. This is also supported by the analysis here based on the response magnitudes. At the surface, the latitudinal gradient in response to ALL (green line in Fig. 5h, − 0.130 K/decade/90° Lat) is about 46% larger than that in response to DV (purple line in Fig. 5h, − 0.089 K/decade/90° Lat), but at 500 hPa ALL gradient is about twice as large as DV gradient (− 0.096 K/decade/90° Lat in ALL vs. -0.050 K/decade/90° Lat in DV, Fig. 5h). In other words, both ALL and DV have large latitudinal gradients near the surface, but the ratio of ALL gradient and DV gradient increases from 1.46 to 1.92 from surface to 500 hPa.

In addition to the magnitude of the linear latitudinal gradient, we further test the robustness of our result by using an alternative way of measuring the hemispheric asymmetry: we calculate the weighted average of zonal mean temperature. The weighting function is defined as: $\omega(\psi) = sin\psi$,

where ψ is latitude. This index is introduced in geoengineering studies (named as "linear latitudinal dependence", Kravitz et al. 2016) and used to emphasize the hemispheric difference of zonal mean temperature trend, which is very suitable for the analysis in this study. Not surprisingly, the linear latitudinal dependence of ZMTT results (Fig. 11a) is highly consistent with the results of the "magnitude" method

(Fig. 11b). At the surface level, the linear latitudinal dependence of ZMTT by NAVI is about half of AA (−0.013 K/decade vs. −0.024 K/decade; note it was −0.092 K/decade/90° Lat vs. 0.101 K/decade/90° Lat in the magnitude method), while at in the mid-troposphere, the dependence caused by NAVI decreases more significantly than AA (−0.005 K/decade for NAVI vs. −0.010 K/decade for AA; −0.033 K/decade/90° Lat vs. −0.069 K/decade/90° Lat in the magnitude method). All the three major methods, as well as the linear latitudinal dependence method mentioned here, reveal the important roles of both AA and NAVI during the mid-20C slowdown period.

5.4 The role of natural forcing and stratospheric ozone

Figure 6e shows the temperature trend pattern at 500 hPa in response to natural-forcing (NAT) during the mid-20C. NAT introduces a global cooling, which is similar to AA but with a smaller magnitude. Notably, the NAT response shows a very small latitudinal gradient (Fig. 6h; − 0.016 K/decade/90°Lat compared with − 0.069 K/decade/90°Lat for AA). Based on horizontal pattern correlation, NAT explains merely 8% of the total variance of the fingerprint of ALL at the 500 hPa level. At the surface level, the NAT again explains only a 7% variance fraction to ALL, which does not change much with altitude. In summary, compared with AA, NAT makes a smaller contribution to the mid-20C cooling and contributes a significantly smaller fraction to the spatial pattern. Also, unlike AA, whose contribution fraction increases with altitude, NAT exhibits a similar variance fraction at different levels.

The vertical pattern of temperature trend induced by NAT is also examined (shown in Fig. 8). The NAT pattern (Fig. 8c) shares some similarities with the AA pattern (Fig. 8e) but with a smaller magnitude at all latitudes and pressure levels, inducing a close-to-zero negative latitudinal gradient (yellow in Fig. 8h). Based on the vertical pattern correlation, NAT explains 34% variance fraction to ALL (per the 2-step attribution framework). The attribution based on vertical patterns shows a more important role of NAT compared with the attribution based on horizontal patterns (Fig. 6), indicating the potentially important role of NAT during the mid-20C. However, the latitudinal gradient induced by NAT is also significantly weaker compared to AA and NAVI_neg at all levels. It is reasonable because the aerosols that originated from volcanic eruptions (especially the two major events in the Northern Hemisphere in 1955 and 1963) contributed to the hemispheric asymmetry of tropospheric temperature, similar to the role of AA; but the volcanic aerosol concentrations decrease quickly after the eruption. Therefore, we conclude that natural forcing from volcanic aerosols should also be considered as the contributors of tropospheric cooling during the mid-20C, but their impact is significantly smaller than NAVI and AA, especially in shaping the observed latitudinal asymmetry.

The stratospheric ozone depletion has also been shown to drive the atmospheric circulation changes in the Southern Hemisphere (Polvani et al. 2011; Marsh et al. 2013). Therefore, the Ozone-only simulations (with a total of 12 realizations) are also examined to test whether Ozone contributes to the latitudinal asymmetry during the mid-20C.

Figure 8f shows the temperature trend pattern at 500 hPa in response to Ozone-only. Overall, ozone induces weak warming globally during the mid-20C (around 0.04 K/decade) but shows no latitudinal gradient (grey lines in Fig. 6h). The vertical pattern of the Ozone-induced temperature trend is also examined in Fig. 8f, which depicts weak warming trends at all levels. The lower levels of SH high latitudes below 850 hPa have stronger warming trends and result in a weak negative latitudinal gradient of temperature trend. The ozone-induced negative gradient is similar to AA and NAT, yet with a much smaller magnitude (by a factor of 3–4 compared to NAT, and a factor of 7 compared to AA; Fig. 8h).

Based on the pattern correlation attribution frameworks (Sects. 5.1 and 5.2), ozone explains near-zero variance fractions to either RE (analysis) or ALL (model response to all forcing) in either horizontal or vertical pattern correlations. Note that it does not necessarily mean the ozone effect can be ignored: focusing on the SH alone, the role of ozone can be important in driving the tropospheric warming in SH, especially the elevated warming in the troposphere. Nevertheless, the focus of this study is to attribute the global latitudinal asymmetry. Thus, we conclude that ozone is not a major contributor to the latitudinal gradient during the mid-20C (1948–1978 as specifically focused here), despite leading to a weak warming trend in the 30° S to 60° S. However, note that ozone induces more significant warming and thus stronger circulation changes in the SH during the latter half of the 20C when the stratospheric ozone depletion is stronger. According to the column stratospheric ozone time series in Fig. S1 of Wang et al. (2020), the drop during 1960–2020 is significantly larger than the decrease during 1948–1978.

Note that the Ozone-only simulations are only available in four of the seven models included in this study (CCSM4, CESM1-CAM5, GISS-E2-R, and GISS-E2-H); thus, the model results with limited ensemble size may contain bias due to model-generated internal variability. Moreover, the CCSM4 and CESM1-CAM5 rely on prescribed stratospheric ozone concentration without interactive chemistry schemes, which could bring additional uncertainties to the ozone results. More importantly, CMIP5 models do not provide simulation to clearly separate the contribution of

stratospheric ozone from tropospheric ozone (also not separated in Polvani et al. 2011). More models with interactive chemistry schemes and more single-forcing simulations (hist-stratO3 experiment) in the ongoing CMIP6 analysis are needed for future analysis focusing on the more recent decades and future recovery of the ozone holes.

5.5 Model uncertainties: the importance of aerosol indirect effects

The seven CMIP5 models applied in this paper include different aerosol-cloud interaction mechanisms, which could partly explain the spread among them. To analyze the model uncertainties, we divide these seven models into three groups in Table 2 based on the aerosol-cloud interactions formulation (Lin et al. 2018). For Group 1 (CCSM4), only the aerosol direct effect is considered. For models in Group 2 (CanESM, GISS-E2-R, and GISS-E2H), parameterized aerosol-cloud interaction is included in the models. The models in Group 3 (CESM1-CAM5, CSIRO-MK3-6–0, and GFDL-CM3) include aerosol-cloud interaction in a prognostic fashion, so aerosols have an even stronger forcing due to the suppression of rainfall efficiency.

Figure 9 compares the spatial patterns of temperature trends in response to ALL and AA experiments at 500 hPa in these three different groups of models. We only show ALL and AA experiments but not GHG because (1) only ALL and AA experiments are affected by aerosol indirect effects, which are the key differences among the three groups, and (2) the climate effects of GHG are well simulated in all models and show very similar results.

Without the aerosol-cloud effect, Group 1 (CCSM4) fails to simulate the mid-20C cooling in the ALL forcing experiment (Fig. 9a), and the latitudinal gradient is not well captured by AA either (red line in Fig. 9h, with latitudinal gradient −0.018 K/decade/90° Lat). On the flip side, ALL in Group 3 (Fig. 9e) shows a nearly opposite pattern compared with Group 1, with near-global cooling. However, the cooling in Group 3 seems to be too strong compared to RE (Fig. 5b), especially over SH mid-latitudes, but the cooling trends over the northern Pacific, Europe, and the northern Atlantic are all consistent with RE. The ALL result of Group 2 (Fig. 9c) most closely resembles the RE, with NH cooling and SH warming, but the cooling over the eastern Pacific is not well captured.

In terms of the magnitude of latitudinal gradients (Fig. 9g–i), Group 1 shows the smallest gradients in both ALL and AA runs while Group 3 has the strongest gradients. Group 3 (blue shading and blue error bar) has larger uncertainty compared with Group 2 in AA runs but smaller uncertainty in ALL. In addition to the 500 hPa shown in Fig. 9, we also do the same analysis for surface (not shown), which largely agrees with 500 hPa, despite the larger bias. Therefore, we argue that the different performances of the three groups of models are consistent from the surface to the mid-troposphere.

In summary, the Group 1 model (CCSM4) fails to simulate the mid-20C slowdown at all due to the lack of aerosol-cloud interaction mechanisms, thus underestimating the overall climate effect of aerosols. However, it is also worth noting that Group 1 only contains one model and three realizations; thus, the remaining internal variability may also bias the results.

On the other hand, by adding the cloud lifetime effect of aerosols, Group 3 models have a significantly stronger aerosol cooling response (with gradient -0.097 ± 0.031 K/decade/90° Lat in the AA run) than Group 2 (-0.073 ± 0.016 K/decade/90° Lat), but the responses seem to be too strong compared to RE. The discrepancy between the three groups demonstrates the importance of aerosol indirect effects in model simulations.

There are concerns that GFDL-CM3 has very high model-generated internal variability compared to other CMIP5 models (Forster et al. 2013; Knutson et al. 2013) so we repeat the horizontal pattern attribution method excluding GFDL-CM3. As anticipated, we find that the contribution of DV to RE decreases (from 21 to 12% at 500 hPa and from 26 to 21% at surface level; original results are shown in Table 4a and b). Despite the quantitative change with or without GFDL-CM3 in the ensemble, our conclusion on the relative roles of ALL and DV still holds.

6 Concluding remarks

It is well documented that the 20th-century global mean temperature features episodic warming slowdown periods (diminished warming or even slight cooling), but the causes, especially a quantitative reconciliation of them, are still being debated. Many studies demonstrate the dominant role of aerosol (e.g., Tett et al. 1999; Haustein et al. 2019), while several studies also emphasize the importance of internal variability (e.g., Maher et al. 2014; Dai et al. 2015). This work provides an updated analysis and brings a new perspective of tropospheric trends. Although with disagreements, all three reanalysis datasets included in this study show a robust latitudinal asymmetry of air temperature trend during the mid-20C, which is supported by homogenized radiosonde product (RAOBCORE). The observed asymmetry from 60°S to 60°N features moderate warming in the SH mid-latitudes, a close-to-zero trend in the tropics, and cooling in the NH mid-latitudes. Our results show that although internal variability partly explains the asymmetry during the slowdown at the surface, the contribution of anthropogenic aerosols to the asymmetry is also important on the surface, and even

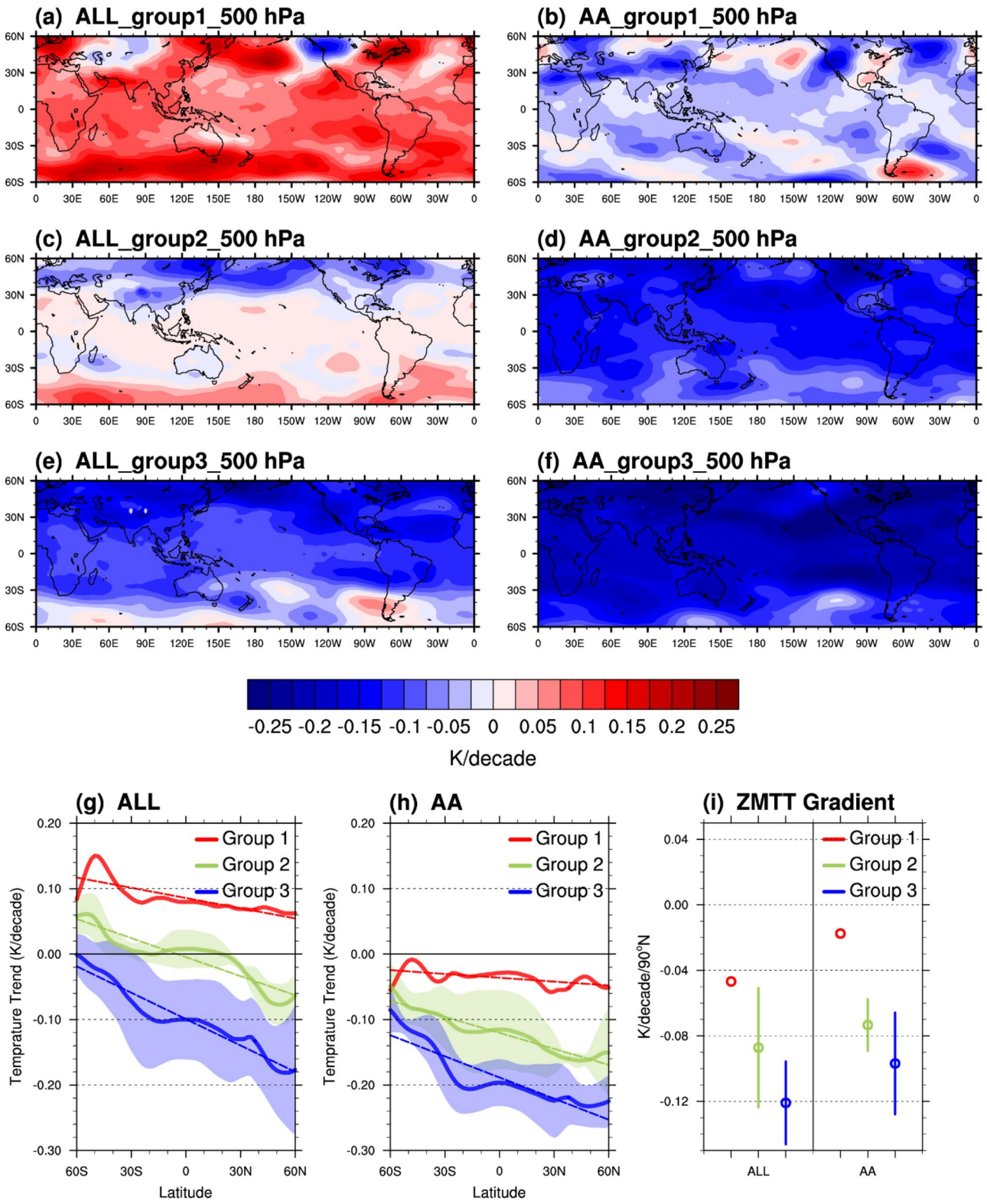

Fig. 9 Similar to Fig. 6 but showing: **a–f** The spatial patterns (60° S–60° N) of the 31-year (1948–1978) linear trend of air temperature at 500 hPa in ALL and AA experiments from three different groups of models (Table 2). **g**, **h** ZMTT at 500 hPa in **g** ALL and **h** AA experiments from three groups of models. The green and blue shadings indicate the standard deviation of the model-to-model difference in Group 2 and Group 3. **i** Latitudinal gradient of ZMTT (K/decade/90° Lat) between 60° S and 60° N. The left part shows results from ALL experiments, while the right part shows results from AA experiments. The green and blue error bars show the standard deviations of model-to-model differences in Groups 2 and 3

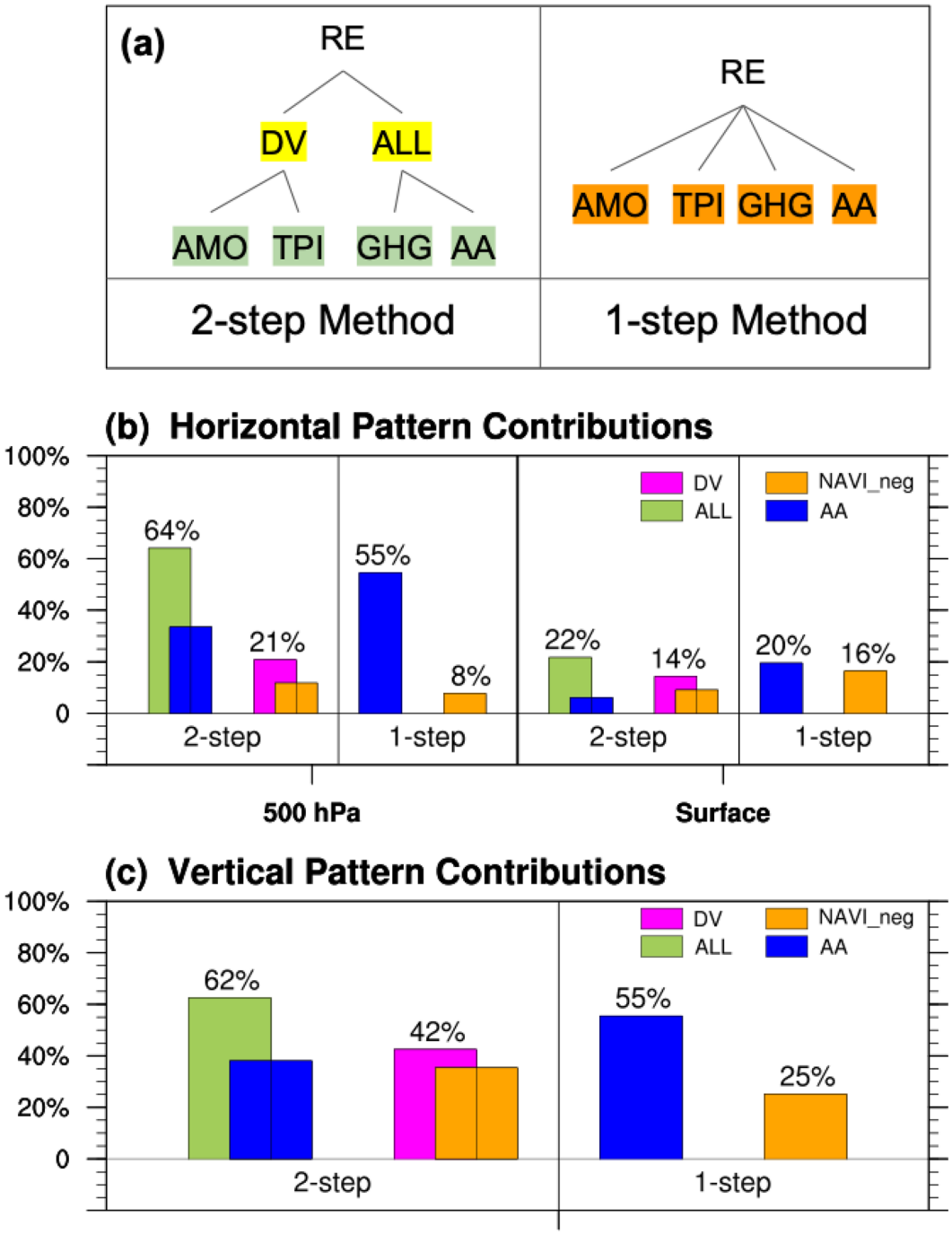

Fig. 10 **a** Two attribution frameworks based on pattern correlation, with the relative contributions summarized in **b**–**d**. GHG and TPI contributions are not shown. The colors here are the same as in Table 4. **b** Attribution of (purple) DV, (green) ALL, (orange) NAVI, and (blue) AA using the horizontal spatial pattern contributions method at (left) 500 hPa and (right) surface. **c** Same as **b** but using the vertical pattern from 1000 to 250 hPa

more so in the mid-troposphere. In this section, we synthesize the findings and draw conclusions.

Based on a 2-step attribution framework (Fig. 10a, left), we quantify the potential roles of internal variability and external forcings based on two different types of pattern correlations, horizontal and vertical (Fig. 10b and c). Our analysis shows that during the mid-20C, both internal variability (DV) and external forcings (ALL) contribute to latitudinal asymmetry, but with different contributions. In terms of DV, the latitudinal asymmetry is mainly driven by the

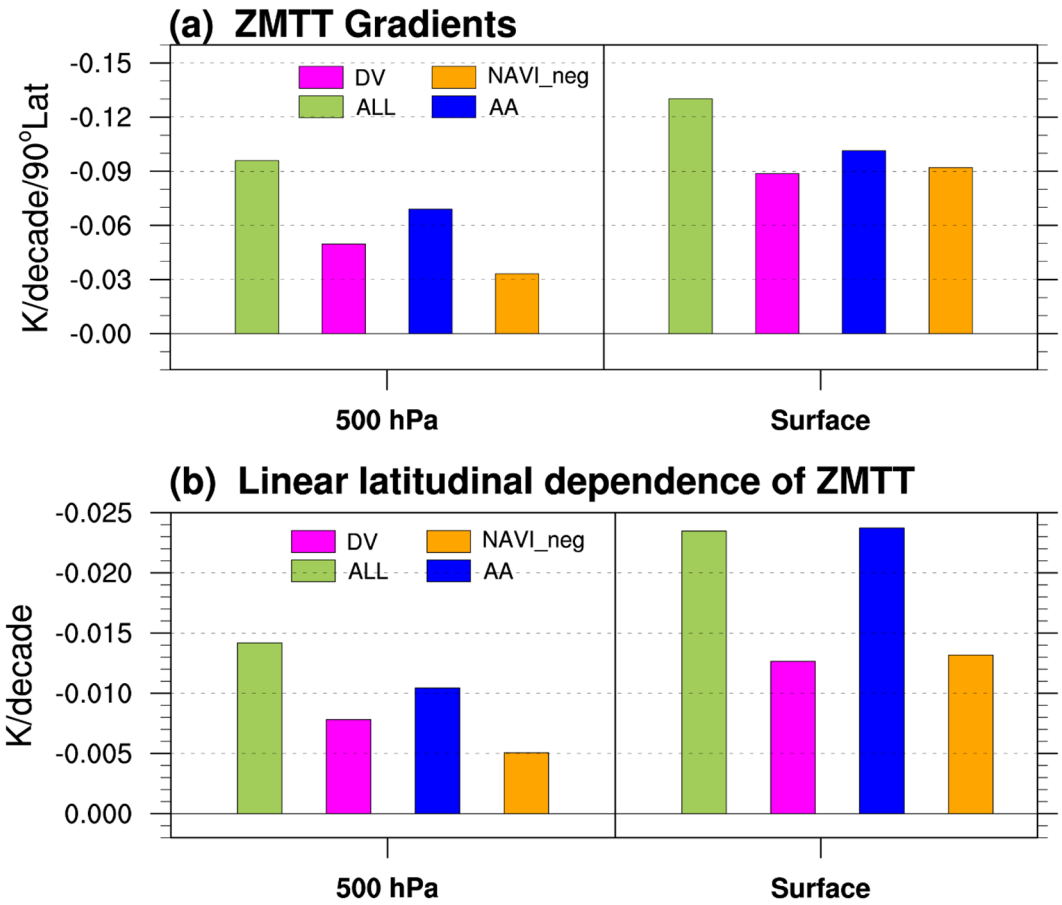

Fig. 11 **a** The ZMTT gradients (60° S–60° N) due to various factors (ALL, DV, AA, and NAVI) at (left) 500 hPa and (right) surface. Negative values indicate greater cooling or weaker warming in the NH compared with the SH. **b** The linear latitudinal dependence of ZMTT (K/decade) from 60° S to 60° N at (left) 500 hPa, and (right) surface using air temperature over the oceans only. Note that negative values indicate greater cooling or weaker warming in the NH relative to the SH

negative transition of NAVI over the Atlantic Ocean during mid-20C (57% at 500 hPa; 63% at the surface; 83% if assessed vertically), but not by TPI, which leads to symmetric patterns. In terms of external forcing, AA is the leading contributor to the asymmetry (52% at 500 hPa; 28% at the surface; 61% if assessed vertically), which offsets the opposite (and weaker) asymmetry caused by GHG concentration increases (Xu and Ramanathan 2012). These latitudinal asymmetries are as expected because AA emissions are concentrated in the NH land regions (mainly causing NH cooling), and the SH is mostly covered by oceans, which are likely to warm or cool more slowly than the land surface.

In addition to the 2-step attribution framework, we also used the 1-step attribution framework (Fig. 10a, right), which directly compares RE with the fingerprints of every single factor. The results from the 1-step framework corroborate the results coming from the 2-step framework in both horizontal pattern contributions (8% by NAVI vs. 55% by AA at 500 hPa; 16 vs. 20% at the surface; Fig. 10a and b) and vertical pattern contributions (25% by NAVI vs. 55% by AA; Fig. 10c), which indicates the robustness of our results.

A key insight from this study is that the contributions of ALL and DV vary greatly with height, according to our analyses based on pattern correlation (Fig. 10b and c) and also based on the magnitude of ZMTT gradients (Fig. 11a). At the surface level, which is the common subject of numerous previous studies, the contribution of DV (14% based on spatial pattern method; −0.09 K/decade/90° Lat based on magnitude method) is similar to external forcings (22%; −0.13 K/decade/90° Lat). However, the contribution of external forcings is much more obvious in the mid-troposphere, accounting for 64% of the observed pattern (−0.10 K/decade/90° Lat based on the magnitude method) compared with the 21% contribution from DV (−0.05 K/decade/90° Lat based on the magnitude method).

Focusing just on the contributions of AA and NAVI, the two leading factors contributing to a global decadal "cooling asymmetry". All approaches yield similar results at the surface level, showing a larger contribution from NAVI than

AA (16 vs. 20% following the 1-step framework; −0.09 K/decade/90° Lat vs. 0.10 K/decade/90° Lat following the magnitude method). But in the mid-troposphere, the contribution of NAVI is smaller than AA (8 vs. 55% following the 1-step framework; −0.03 K/decade/90° Lat vs. −0.07 K/decade/90° Lat following the magnitude method). The reason why AA contribution is more pronounced in the mid-troposphere than NAVI is that AA can impose direct energy imbalance onto the troposphere in addition to the slow bottom-up response due to SST pattern (e.g., see a decomposition of fast and slow components in response to AA in Wang et al. 2017). Therefore, with a focus on the tropospheric air temperature as the attribution target, we identify a stronger and more dominant role of AA, compared to the weaker role found for surface temperature and precipitation as noted in previous studies (e.g., Knight et al. 2006; Maher et al. 2014). Moreover, by looking at the entire low- to mid-troposphere up to 250 hPa (Fig. 10c), external forcings overall make a larger contribution to the ZMTT gradient compared to DV (62% for ALL vs. 42% for DV).

The natural forcing (NAT) also contributes to the mid-20C cooling asymmetry, yet with much smaller fractions (−0.016 K/decade/90° Lat of ZMTT at 500 hPa; explains 7% variance of ALL on the surface following 2-step framework) compared to AA and NAVI.

Lastly, we share thoughts on future research directions.

- This paper mainly focuses on the mid-20C (1948–1978), where the relative roles of aerosol emissions and the NAVI transition are profound and in the same direction. Similar analyses could also be performed for the more recent periods considering the different aerosol emission spatial patterns and temporal trends, such as the early-21C warming slowdown (1998–2013) or the rapid warming period during 1978–1998.
- In addition to the three reanalysis datasets included in the study, the extension of the ECMWF Reanalysis v5 (ERA5; Bell et al. 2020) product is ongoing and will cover the focused period soon. Analysis based on such newly developed reanalysis datasets is worth conducting to further explore the uncertainty of reanalysis products.
- In addition to CMIP5, the CMIP6 simulations have recently become available. CMIP6, compared with CMIP5, provides more single-forcing simulations (approximately 100 individual runs of aerosol-only), allowing better capability in separating externally induced climate responses from natural variabilities. Nevertheless, it shows that the 21-member ensemble from CMIP5 is large enough to separate the externally forced climate responses from the model-generated internal variability; thus, we defer CMIP6 simulations to future studies.

Despite the overall improvement in many aspects of simulating climatology and variability, some recent studies argued that many CMIP6 models overestimate the aerosol forcings, and consequently produce cooling bias during the mid-20th century compared to observation (Gettelman et al. 2019; Zelinka et al. 2020). The source of this issue is under active investigation. Therefore, in this study, we rely on the well-documented CMIP5 output and build our troposphere-focused analysis on previous studies on surface climate trends. Further diagnostics on the issue of model sensitivity due to more diverse aerosol representation in the CMIP6 class are warranted in the future.

- Here we adopt an alternative index of NAVI to mitigate the entanglement of external forcing and internal variability (at least for AA and Atlantic variability) to assess their individual contributions in driving the observed climate trend at a decadal time scale. However, we do note that a clean separation in any given period is difficult. For example, some other studies demonstrated that the externally forced signal, especially from the regional forcing of aerosols, can reflect on or even excite internal modes (Smith et al. 2011, 2016; Allen et al. 2014; Takahashi and Watanabe 2016). Previous work (Xu and Hu 2018) also showed a potentially detectable GHG impact on PDO/IPO when the warming level is high in the future.
- The role of ozone is examined in this study, showing no contribution to the mid-20C cooling asymmetry. However, the analysis is only based on the stratospheric and tropospheric ozone-only simulations included in CMIP5, with limited ensemble sizes. Future analysis is needed to further justify the separate contributions of stratospheric ozone and tropospheric ozone. Larger ensemble sizes and models with advanced chemical schemes, such as in CMIP5, will be helpful to narrow the uncertainties of ozone contributions to the climate.
- Here we also highlight the importance of looking beyond the surface climate by analyzing the tropospheric air temperature, and we encourage future detailed analysis of additional variables or dynamic mechanisms [e.g., ocean heat content (Delworth et al. 2005), atmospheric circulation (Xu and Xie 2015), ocean circulation (Verma et al. 2019)].

Supplementary Information The online version contains supplementary material available at https://doi.org/10.1007/s00382-022-06235-y.

Acknowledgements We thank Steven Schroeder for his comments on an earlier draft. We acknowledge the World Climate Research Programme's Working Group on Coupled Modelling, which is responsible for CMIP, and we thank the climate modeling groups (listed in Table 2 of this paper) for producing and making available the model output.

Access to the CMIP5 data and technical assistance is provided by the German Climate Computing Centre (DKRZ). We acknowledge NCAR for the high-performance computing support from Cheyenne (https://doi.org/10.5065/D6RX99HX) and the data storage resources provided by Computational and Information Systems Laboratory (CISL).

Funding This study is supported by the National Science Foundation under Award No. AGS-1841308.

Data availabilty statement Enquiries about data availability should be directed to the authors.

Declarations

Conflict of interest The authors have not disclosed any competing interests.

References

Allen RJ, Norris JR, Kovilakam M (2014) Influence of anthropogenic aerosols and the Pacific Decadal Oscillation on tropical belt width. Nat Geosci 7:270–274. https://doi.org/10.1038/ngeo2091

Allen RJ, Evan AT, Booth BBB (2015) Interhemispheric aerosol radiative forcing and tropical precipitation shifts during the late twentieth century. J Clim 28:8219–8246. https://doi.org/10.1175/JCLI-D-15-0148.1

An S-I, Shin J, Yeh S-W et al (2021) Global cooling hiatus driven by an AMOC overshoot in a carbon dioxide removal scenario. J Med Sci 9:e2021EF002165. https://doi.org/10.1029/2021EF002165

Bell B, Hersbach H, Berrisford P et al (2020) ERA5 hourly data on single levels from 1950 to 1978 (preliminary version). In: Copernicus climate change service climate data store. https://cds.climate.copernicus.eu/cdsapp#!/dataset/reanalysis-era5-single-levels-preliminary-back-extension?tab=overview. Accessed 17 Dec 2021

Bindoff NL, Stott PA, AchutaRao KM et al (2013) Detection and attribution of climate change: from global to regional. In: Stocker TF, Qin D, Plattner G-K et al (eds) Climate change 2013: The physical science basis. Contribution of working group I to the fifth assessment report of the intergovernmental panel on climate change. Cambridge University Press, Cambridge, pp 867–952

Booth BBB, Dunstone NJ, Halloran PR et al (2012) Aerosols implicated as a prime driver of twentieth-century North Atlantic climate variability. Nature 484:228–232. https://doi.org/10.1038/nature10946

Brohan P, Kennedy JJ, Harris I et al (2006) Uncertainty estimates in regional and global observed temperature changes: a new data set from 1850. J Geophys Res 111:D12106. https://doi.org/10.1029/2005JD006548

Cai W, Bi D, Church J et al (2006) Pan-oceanic response to increasing anthropogenic aerosols: impacts on the Southern Hemisphere oceanic circulation. Geophys Res Lett 33:L21707. https://doi.org/10.1029/2006GL027513

Chang C-Y, Chiang JCH, Wehner MF et al (2010) Sulfate aerosol control of tropical Atlantic climate over the twentieth century. J Clim 24:2540–2555. https://doi.org/10.1175/2010JCLI4065.1

Chen X, Tung KK (2018) Global surface warming enhanced by weak Atlantic overturning circulation. Nature 559:387–391. https://doi.org/10.1038/s41586-018-0320-y

Cheng L, Zhu J (2014) Artifacts in variations of ocean heat content induced by the observation system changes. Geophys Res Lett 41:7276–7283. https://doi.org/10.1002/2014GL061881

Chiang JCH, Friedman AR (2012) Extratropical cooling, interhemispheric thermal gradients, and tropical climate change. Annu Rev Earth Planet Sci 40:383–412. https://doi.org/10.1146/annurev-earth-042711-105545

Chung E-S, Soden BJ (2017) Hemispheric climate shifts driven by anthropogenic aerosol–cloud interactions. Nat Geosci 10:566–571. https://doi.org/10.1038/ngeo2988

Chylek P, Li J, Dubey MK et al (2011) Observed and model simulated 20th century Arctic temperature variability: Canadian Earth System Model CanESM2. Atmos Chem Phys Discuss 2011:22893–22907. https://doi.org/10.5194/acpd-11-22893-2011

Chylek P, Dubey MK, Lesins G et al (2014) Imprint of the Atlantic multi-decadal oscillation and Pacific decadal oscillation on southwestern US climate: past, present, and future. Clim Dyn 43:119–129. https://doi.org/10.1007/s00382-013-1933-3

Collier MA, Jeffrey SJ, Rotstayn LD et al (2011) The CSIRO-Mk3.6.0 Atmosphere-Ocean GCM: participation in CMIP5 and data publication. In: Proceedings of MODSIM 2011 international congress on modelling and simulation, p 2691–2697

Compo GP, Whitaker JS, Sardeshmukh PD et al (2011) The twentieth century reanalysis project. Q J R Meteorol Soc 137:1–28. https://doi.org/10.1002/qj.776

Cowtan K, Way RG (2014) Coverage bias in the HadCRUT4 temperature series and its impact on recent temperature trends. Q J R Meteorol Soc 140:1935–1944. https://doi.org/10.1002/qj.2297

Dai A, Fyfe JC, Xie SP, Dai X (2015) Decadal modulation of global surface temperature by internal climate variability. Nat Clim Chang 5:555. https://doi.org/10.1038/nclimate2605

Delworth TL, Ramaswamy V, Stenchikov GL (2005) The impact of aerosols on simulated ocean temperature and heat content in the 20th century. Geophys Res Lett. https://doi.org/10.1029/2005GL024457

Dong B, Dai A (2015) The influence of the interdecadal Pacific oscillation on temperature and precipitation over the globe. Clim Dyn 45:2667–2681. https://doi.org/10.1007/s00382-015-2500-x

Dong L, McPhaden MJ (2017) The role of external forcing and internal variability in regulating global mean surface temperatures on decadal timescales. Environ Res Lett 12:034011. https://doi.org/10.1088/1748-9326/aa5dd8

Dong L, Zhou T, Chen X (2014) Changes of Pacific decadal variability in the twentieth century driven by internal variability, greenhouse gases, and aerosols. Geophys Res Lett. https://doi.org/10.1002/2014GL062269

Easterling DR, Wehner MF (2009) Is the climate warming or cooling? Geophys Res Lett 36(8):L08706. https://doi.org/10.1029/2009GL037810

Emile-Geay J, Seager R, Cane MA et al (2008) Volcanoes and ENSO over the past millennium. J Clim 21:3134–3148. https://doi.org/10.1175/2007JCLI1884.1

Evan AT, Vimont DJ, Heidinger AK et al (2009) The role of aerosols in the evolution of tropical North Atlantic ocean temperature anomalies. Science (80-) 324:778–781. https://doi.org/10.1126/science.1167404

Flato G, Marotzke J, Abiodun B et al (2013) Evaluation of Climate Models. In: Clim I (ed) Climate change 2013—the physical science basis. Cambridge University Press, Cambridge, pp 741–866

Forster PM, Andrews T, Good P et al (2013) Evaluating adjusted forcing and model spread for historical and future scenarios in the CMIP5 generation of climate models. J Geophys Res Atmos 118:1139–1150. https://doi.org/10.1002/jgrd.50174

Foster G, Rahmstorf S (2011) Global temperature evolution 1979–2010. Environ Res Lett 6:044022. https://doi.org/10.1088/1748-9326/6/4/044022

Friedman AR, Hwang YT, Chiang JCH, Frierson DMW (2013) Interhemispheric temperature asymmetry over the twentieth century

and in future projections. J Clim 26:5419–5433. https://doi.org/10.1175/JCLI-D-12-00525.1
Fyfe JC, Meehl GA, England MH et al (2016) Making sense of the early-2000s warming slowdown. Nat Clim Chang 6:224–228
Fyfe JC, Derksen C, Mudryk L et al (2017) Large near-term projected snowpack loss over the western United States. Nat Commun 8:14996. https://doi.org/10.1038/ncomms14996
Gettelman A, Hannay C, Bacmeister JT, Neale RB, Pendergrass AG, Danabasoglu G, Lamarque J-F, Fasullo JT, Bailey DA, Lawrence DM, Mills MJ (2019) High climate sensitivity in the community earth system model version 2 (CESM2). Geophys Res Lett 46(14):8329–8337. https://doi.org/10.1029/2019GL083978
Gent PR, Danabasoglu G, Donner LJ et al (2011) The community climate system model version 4. J Clim 24:4973–4991. https://doi.org/10.1175/2011JCLI4083.1
Gillett NP, Kirchmeier-Young M, Ribes A et al (2021) Constraining human contributions to observed warming since the pre-industrial period. Nat Clim Chang. https://doi.org/10.1038/s41558-020-00965-9
Griffies SM, Winton M, Donner LJ et al (2011) The GFDL CM3 coupled climate model: characteristics of the ocean and sea Ice simulations. J Clim 24:3520–3544. https://doi.org/10.1175/2011JCLI3964.1
Haustein K, Otto FEL, Venema V et al (2019) A limited role for unforced internal variability in twentieth-century warming. J Clim 32:4893–4917. https://doi.org/10.1175/JCLI-D-18-0555.1
Henley BJ, Gergis J, Karoly DJ et al (2015) A tripole index for the interdecadal Pacific Oscillation. Clim Dyn 45:3077–3090. https://doi.org/10.1007/s00382-015-2525-1
Hwang YT, Frierson DMW, Kang SM (2013) Anthropogenic sulfate aerosol and the southward shift of tropical precipitation in the late 20th century. Geophys Res Lett 40:2845–2850. https://doi.org/10.1002/grl.50502
Jones GS, Stott PA, Christidis N (2013) Attribution of observed historical near-surface temperature variations to anthropogenic and natural causes using CMIP5 simulations. J Geophys Res Atmos 118:4001–4024. https://doi.org/10.1002/jgrd.50239
Kalnay E, Kanamitsu M, Kistler R et al (1996) The NCEP/NCAR 40-year reanalysis project. Bull Am Meteorol Soc 77:437–471. https://doi.org/10.1175/1520-0477(1996)077%3c0437:TNYRP%3e2.0.CO;2
Karl TR, Arguez A, Huang B et al (2015) Possible artifacts of data biases in the recent global surface warming hiatus. Science 348:1469–1472. https://doi.org/10.1126/science.aaa5632
Kistler R, Collins W, Saha S et al (2001) The NCEP–NCAR 50–year reanalysis: monthly means CD–ROM and documentation. Bull Am Meteorol Soc 82:247–267. https://doi.org/10.1175/1520-0477(2001)082%3c0247:TNNYRM%3e2.3.CO;2
Knight JR, Folland CK, Scaife AA (2006) Climate impacts of the Atlantic multidecadal oscillation. Geophys Res Lett 33:L17706. https://doi.org/10.1029/2006GL026242
Knutson TR, Zeng F, Wittenberg AT (2013) Multimodel assessment of regional surface temperature trends: CMIP3 and CMIP5 twentieth-century simulations. J Clim 26:8709–8743. https://doi.org/10.1175/JCLI-D-12-00567.1
Kobayashi S, Ota Y, Harada Y et al (2015) The JRA-55 reanalysis: general specifications and basic characteristics. J Meteorol Soc Jpn Ser II 93:5–48. https://doi.org/10.2151/jmsj.2015-001
Kosaka Y, Xie S-P (2013) Recent global-warming hiatus tied to equatorial Pacific surface cooling. Nature 501:403–407. https://doi.org/10.1038/nature12534
Kostov Y, Armour KC, Marshall J (2014) Impact of the Atlantic meridional overturning circulation on ocean heat storage and transient climate change. Geophys Res Lett 41:2108–2116. https://doi.org/10.1002/2013GL058998
Kravitz B, MacMartin DG, Wang H, Rasch PJ (2016) Geoengineering as a design problem. Earth Syst Dyn 7:469–497. https://doi.org/10.5194/esd-7-469-2016
Laloyaux P, Balmaseda M, Dee D et al (2016) A coupled data assimilation system for climate reanalysis. Q J R Meteorol Soc 142:65–78. https://doi.org/10.1002/qj.2629
Le T (2017) ENSO response to external forcing in CMIP5 simulations of the last millennium. Glob Planet Change 148:105–112. https://doi.org/10.1016/j.gloplacha.2016.12.002
Lee YH, Pierce JR, Adams PJ (2013) Representation of nucleation mode microphysics in a global aerosol model with sectional microphysics. Geosci Model Dev 6:1221–1232. https://doi.org/10.5194/gmd-6-1221-2013
Lin L, Xu Y, Wang Z et al (2018) Changes in extreme rainfall over India and China attributed to regional aerosol-cloud interaction during the late 20th century rapid industrialization. Geophys Res Lett 45:7857–7865. https://doi.org/10.1029/2018GL078308
Liu J, Rühland KM, Chen J et al (2017) Aerosol-weakened summer monsoons decrease lake fertilization on the Chinese Loess Plateau. Nat Clim Chang 7:190–194. https://doi.org/10.1038/nclimate3220
Maher N, Sen GA, England MH (2014) Drivers of decadal hiatus periods in the 20th and 21st centuries. Geophys Res Lett 41:5978–5986. https://doi.org/10.1002/2014GL060527
Mann ME, Steinman BA, Miller SK (2014) On forced temperature changes, internal variability, and the AMO. Geophys Res Lett 41:3211–3219. https://doi.org/10.1002/2014GL059233
Mantua NJ, Hare SR (2002) The Pacific decadal oscillation. J Oceanogr 58:35–44. https://doi.org/10.1023/A:1015820616384
Marsh DR, Mills MJ, Kinnison DE et al (2013) Climate change from 1850 to 2005 simulated in CESM1(WACCM). J Clim 26:7372–7391. https://doi.org/10.1175/JCLI-D-12-00558.1
McGregor S, Timmermann A, Stuecker MF et al (2014) Recent Walker circulation strengthening and Pacific cooling amplified by Atlantic warming. Nat Clim Chang 4:888–892. https://doi.org/10.1038/nclimate2330
Medhaug I, Stolpe MB, Fischer EM, Knutti R (2017) Reconciling controversies about the 'global warming hiatus.' Nature 545:41–47. https://doi.org/10.1038/nature22315
Meehl GA, Hu A, Santer BD (2009) The mid-1970s climate shift in the pacific and the relative roles of forced versus inherent decadal variability. J Clim 22:780–792. https://doi.org/10.1175/2008JCLI2552.1
Meehl GA, Hu A, Arblaster JM et al (2013a) Externally forced and internally generated decadal climate variability associated with the interdecadal Pacific oscillation. J Clim 26:7298–7310. https://doi.org/10.1175/JCLI-D-12-00548.1
Meehl GA, Washington WM, Arblaster JM et al (2013b) Climate change projections in CESM1(CAM5) compared to CCSM4. J Clim 26:6287–6308. https://doi.org/10.1175/JCLI-D-12-00572.1
Newman M, Alexander MA, Ault TR et al (2016) The pacific decadal oscillation, revisited. J Clim 29:4399–4427. https://doi.org/10.1175/JCLI-D-15-0508.1
Ocko IB, Ramaswamy V, Ming Y (2014) Contrasting climate responses to the scattering and absorbing features of anthropogenic aerosol forcings. J Clim 27:5329–5345. https://doi.org/10.1175/JCLI-D-13-00401.1
Otterå OH, Bentsen M, Drange H, Suo L (2010) External forcing as a metronome for Atlantic multidecadal variability. Nat Geosci 3:688–694. https://doi.org/10.1038/ngeo955
Polvani LM, Waugh DW, Correa GJP, Son S-W (2011) Stratospheric ozone depletion: the main driver of twentieth-century atmospheric circulation changes in the Southern Hemisphere. J Clim 24:795–812. https://doi.org/10.1175/2010JCLI3772.1

Rahmstorf S, Foster G, Cahill N (2017) Global temperature evolution: recent trends and some pitfalls. Environ Res Lett 12:054001. https://doi.org/10.1088/1748-9326/aa6825

Ribes A, Planton S, Terray L (2013) Application of regularised optimal fingerprinting to attribution. Part I: method, properties and idealised analysis. Clim Dyn. https://doi.org/10.1007/s00382-013-1735-7

Risbey JS, Lewandowsky S, Cowtan K et al (2018) A fluctuation in surface temperature in historical context: reassessment and retrospective on the evidence. Environ Res Lett 13:123008. https://doi.org/10.1088/1748-9326/aaf342

Schlesinger ME, Ramankutty N (1994) An oscillation in the global climate system of period 65–70 years. Nature 367:723–726. https://doi.org/10.1038/367723a0

Schneider N, Cornuelle BD (2005) The forcing of the Pacific decadal oscillation. J Clim 18:4355–4373. https://doi.org/10.1175/JCLI3527.1

Smith SJ, van Aardenne J, Klimont Z et al (2011) Anthropogenic sulfur dioxide emissions: 1850–2005. Atmos Chem Phys 11:1101–1116. https://doi.org/10.5194/acp-11-1101-2011

Smith DM, Booth BBB, Dunstone NJ et al (2016) Role of volcanic and anthropogenic aerosols in the recent global surface warming slowdown. Nat Clim Chang 6:936–940. https://doi.org/10.1038/nclimate3058

Smith CJ, Kramer RJ, Myhre G et al (2018) Understanding rapid adjustments to diverse forcing agents. Geophys Res Lett 45:12,023-12,031. https://doi.org/10.1029/2018GL079826

Sun Y, Zhang X, Ren G et al (2016) Contribution of urbanization to warming in China. Nat Clim Chang 6:706–709. https://doi.org/10.1038/nclimate2956

Takahashi C, Watanabe M (2016) Pacific trade winds accelerated by aerosol forcing over the past two decades. Nat Clim Chang 6:768–772. https://doi.org/10.1038/nclimate2996

Tett SFB, Stott PA, Allen MR et al (1999) Causes of twentieth-century temperature change near the Earth's surface. Nature 399:569–572. https://doi.org/10.1038/21164

Tett SFB, Jones GS, Stott PA et al (2002) Estimation of natural and anthropogenic contributions to twentieth century temperature change. J Geophys Res 107:4306. https://doi.org/10.1029/2000JD000028

Thompson DWJ, Wallace JM, Kennedy JJ, Jones PD (2010) An abrupt drop in Northern Hemisphere sea surface temperature around 1970. Nature 467:444–447. https://doi.org/10.1038/nature09394

Trenberth KE, Hurrell JW (1994) Decadal atmosphere-ocean variations in the Pacific. Clim Dyn 9:303–319. https://doi.org/10.1007/BF00204745

Tung K-K, Chen X (2018) Understanding the recent global surface warming slowdown: a review. Climate 6:82. https://doi.org/10.3390/cli6040082

Verma T, Saravanan R, Chang P, Mahajan S (2019) Tropical Pacific ocean dynamical response to short-term sulfate aerosol forcing. J Clim 32:8205–8221. https://doi.org/10.1175/JCLI-D-19-0050.1

Wang Z, Lin L, Yang M et al (2017) Disentangling fast and slow responses of the East Asian summer monsoon to reflecting and absorbing aerosol forcings. Atmos Chem Phys 17:11075–11088. https://doi.org/10.5194/acp-17-11075-2017

Wang H, Xie S-P, Zheng X-T et al (2020) Dynamics of Southern Hemisphere atmospheric circulation response to anthropogenic aerosol forcing. Geophys Res Lett 47:e2020GL089919. https://doi.org/10.1029/2020GL089919

Wu S, Liu Z, Zhang R, Delworth TL (2011) On the observed relationship between the Pacific decadal oscillation and the Atlantic multi-decadal oscillation. J Oceanogr 67:27–35. https://doi.org/10.1007/s10872-011-0003-x

Xu Y, Hu A (2018) How would the twenty-first-century warming influence Pacific decadal variability and its connection to North American rainfall: assessment based on a revised procedure for the IPO/PDO. J Clim 31:1547–1563. https://doi.org/10.1175/JCLI-D-17-0319.1

Xu Y, Ramanathan V (2012) Latitudinally asymmetric response of global surface temperature: implications for regional climate change. Geophys Res Lett. https://doi.org/10.1029/2012GL052116

Xu Y, Xie S-P (2015) Ocean mediation of tropospheric response to reflecting and absorbing aerosols. Atmos Chem Phys 15:5827–5833. https://doi.org/10.5194/acp-15-5827-2015

Yan X, Boyer T, Trenberth K et al (2016) The global warming hiatus: slowdown or redistribution? Earth's Futur 4:472–482. https://doi.org/10.1002/2016EF000417

Yao B, Xu Y, Dessler AE, Liu C (2021) Characterizing unforced decadal climate variability in global climate model large ensembles. Clim Dyn. https://doi.org/10.1007/s00382-021-05900-y

Zelinka MD, Myers TA, McCoy DT, Po-Chedley S, Caldwell PM, Ceppi P, Klein SA, Taylor KE (2020) Causes of higher climate sensitivity in CMIP6 models. Geophys Res Lett 47(1):e2019GL085782. https://doi.org/10.1029/2019GL085782

Zhang R, Sutton R, Danabasoglu G et al (2019) A review of the role of the Atlantic meridional overturning circulation in Atlantic multidecadal variability and associated climate impacts. Rev Geophys 57:316–375. https://doi.org/10.1029/2019RG000644